Water Vapor Fluxes and Orographic Precipitation over Northern California Associated with a Landfalling Atmospheric River

BARRETT L. SMITH* AND SANDRA E. YUTER

Department of Marine, Earth, and Atmospheric Sciences, North Carolina State University, Raleigh, North Carolina

PAUL J. NEIMAN

NOAA/Earth System Research Laboratory, Boulder, Colorado

D. E. KINGSMILL

University of Colorado, CIRES, and NOAA/Earth System Research Laboratory, Boulder, Colorado

(Manuscript received 8 January 2009, in final form 23 June 2009)

ABSTRACT

Atmospheric rivers accompanying Pacific storm systems play an important role in supplying moisture to the West Coast. Heavy precipitation associated with these systems falls not only along the west-facing slopes of the Coastal Range but also along the windward slopes of the interior Sierra Mountains. Simulations of the 29–31 December 2005 storm in northern California using the Weather Research and Forecasting (WRF) model were able to realistically resolve the structure and strength of the water vapor fluxes over ocean and land. The cross-barrier, southwesterly water vapor fluxes, peaking near 700 kg m^{-1} s^{-1} at the coast, dominated the airmass transformation over the northern California mountain complex. However, there was also significant northward water vapor flux along the base of the Sierras. The combination of a narrow, short-lived water vapor source from the atmospheric river, the gap in terrain facilitating flow around the coastal mountains, and the occurrence of a strong barrier jet at the base of the Sierras all contributed to the northward along-barrier water vapor fluxes within the storm. The coincident timing of the maximum water vapor flux into the central valley with the period when the barrier jet was well developed yielded up valley fluxes $>$300 kg m^{-1} s^{-1} for several hours. For the 29–31 December 2005 Pacific storm, the flow around the coastal terrain and up valley replenished about a quarter of the depleted water vapor lost over the coastal mountains.

1. Introduction

Over the last three decades, several field projects have provided invaluable insight into the development of heavy precipitation along the west coast of North America. The Sierra Cooperative Pilot Project (SCPP; Reynolds and Dennis 1986) was the first to investigate how a wide spectrum of synoptic patterns and storms evolved as they interacted with the terrain. Storms with west-to-southwesterly flow were found to be associated with the heaviest precipitation. SCPP also documented the terrain-enhanced barrier-jet winds (Parish 1982; Marwitz 1983, 1986, 1987) and microphysical structures over the terrain (e.g., Heggli and Rauber 1988; Rauber 1992). During the Coastal Observations and Simulation with Topography (COAST) I and II experiments (Bond et al. 1997), observations of frontal systems approaching coastal topography provided insight into the modification of fronts (Braun et al. 1999a,b) and the development of barrier flows.

The California Landfalling Jets Experiment (CALJET) and the Pacific Landfalling Jets Experiment (PACJET; Ralph et al. 1999; Neiman et al. 2002, 2005) investigated the prefrontal low-level jet (LLJ) associated with Pacific storm systems. The LLJ, which forms in response to restoring thermal wind balance, can lead to extreme flooding when it transports water vapor toward a mountain range (Buzzi et al. 1998; Doswell et al. 1998; Lin et al.

* Current affiliation: National Weather Service, Raleigh, North Carolina.

Corresponding author address: Dr. Sandra E. Yuter, Department of Marine, Earth, and Atmospheric Sciences, North Carolina State University, Raleigh, NC 27695.
E-mail: seyuter@ncsu.edu

DOI: 10.1175/2009MWR2939.1

2001; Rotunno and Ferretti 2001; White et al. 2003; Ralph et al. 2004, 2005; Neiman et al. 2008). Ralph et al. (2004) used dropsonde and satellite data from CALJET to describe the characteristics of the LLJ and strong water vapor transport associated with southwesterly flow. The baroclinicity of Pacific storms was found to enhance the prefrontal LLJ, which often forms near the 900-hPa level in the precold-frontal warm sector ahead of midlatitude cyclones. These findings are consistent with those of Lackmann and Gyakum (1999), who found that the low-level southwesterly flow and water vapor transport associated with Pacific storms is enhanced by the interaction of Pacific low pressure systems and an anticyclone located downstream off the Southwest coast.

Collocated with the LLJ is a narrow region, on the order of 500 km wide, of enhanced water vapor content. This plume of water vapor, also known as an atmospheric river (Zhu and Newell 1998), lies within the warm conveyor belt present in many midlatitude cyclones crossing the United States (Carlson 1980; Browning 1990, Ralph et al. 2004). Bao et al. (2006) used back trajectory analysis to interpret the formation of enhanced vertically integrated water vapor bands in the central and eastern Pacific. Under a subset of environmental conditions, they were able to trace the moisture back from the coast of California to the tropics. More typically it was local moisture convergence that was primarily responsible for the formation of the enhanced water vapor bands. Atmospheric rivers do not represent true trajectories of the core region of water vapor transport. Rather, they depict the instantaneous position of corridors of enhanced water vapor flux, typically focused in the lower troposphere below ~700 hPa and in the portion of the warm conveyor belt near the leading edge of the polar cold front. Similarly, jet streams/jet streaks are instantaneous snapshots of corridors of enhanced flow rather than a trajectory perspective of these flow features.

The majority of water vapor in the atmospheric river is located below 2.25-km altitude (Ralph et al. 2005). A single atmospheric river can extend for thousands of kilometers from the tropics into the midlatitudes. There are typically four to five atmospheric rivers present across the Northern Hemisphere at any time, and these rivers are responsible for ~90% of the meridional water vapor transport at midlatitudes (Zhu and Newell 1998; Ralph et al. 2004). Atmospheric rivers play a key role in water vapor availability for precipitation processes within midlatitude cyclones, and the proximity of the mountainous terrain of the western United States to this water vapor source is ideal for episodes of heavy orographic precipitation.

Neiman et al. (2008) used 8 yr of Special Sensor Microwave Imager (SSM/I) data (1998–2005) to examine the characteristics and landfalling impacts of atmospheric rivers over the northeastern Pacific Ocean. Wintertime systems were associated with a deep trough over the eastern Pacific with enhanced low-level baroclinicity and a polar cold front extending from northeast to southwest toward the tropics. Although wintertime atmospheric rivers contained less water vapor than those in summer, the storm dynamics of wintertime storms, specifically the LLJ, were stronger. Thus, the horizontal water vapor flux directed toward the coastal terrain associated with winter atmospheric rivers was stronger than in summer, leading to more orographic precipitation during the winter.

The interactions of blocked and unblocked flow by the terrain in a given storm have significant consequences on the amount of water vapor that is able to penetrate the Sacramento Valley and on how much precipitation falls along the windward Sierra slopes. Galewsky and Sobel (2005) studied the 1997 New Year's Flood, which was a potent case of a Pacific cyclone and attendant atmospheric river. High θ_e air flowed over the northern Coastal Ranges while low θ_e air moved into the northern central valley from the south on a range-parallel barrier jet. The interaction of these high and low θ_e flows enhanced precipitation in the northern Sierra by creating a blanket of low θ_e air over which the moist air was uplifted. Galewsky and Sobel's results for their case study were similar to Rotunno and Ferretti's (2001) idealized simulations, which found that the convergence of high and low θ_e air produced stronger vertical motions and higher rain rates than simple orographic uplift.

In this study, we build on the previous work to quantify the water vapor fluxes of flow over and around the northern California mountain complex in atmospheric river conditions. In particular, we examine the numerically simulated water vapor fluxes into and out of strategically placed boxes in order to quantify both the cross-barrier and along-barrier airmass transformation over the region. The design of the water budgets incorporated in this study was based on the spatial orientation of both the environmental phenomenon of interest, which was the atmospheric river, and the terrain of California.

Our goal is to investigate the three-dimensional changes in water vapor flux associated with an atmospheric river (i.e., a narrow plume of strong horizontal water vapor flux) as it moves over the northern California mountain complex composed of the Coastal Ranges and the Sierra Nevada (Fig. 1). We utilize mesoscale model simulations to estimate water vapor fluxes during the 29–31 December 2005 storm and to test their sensitivity to different mountain topography configurations. This slow-moving storm had significant impacts in the region, is well documented, and has been analyzed in past studies

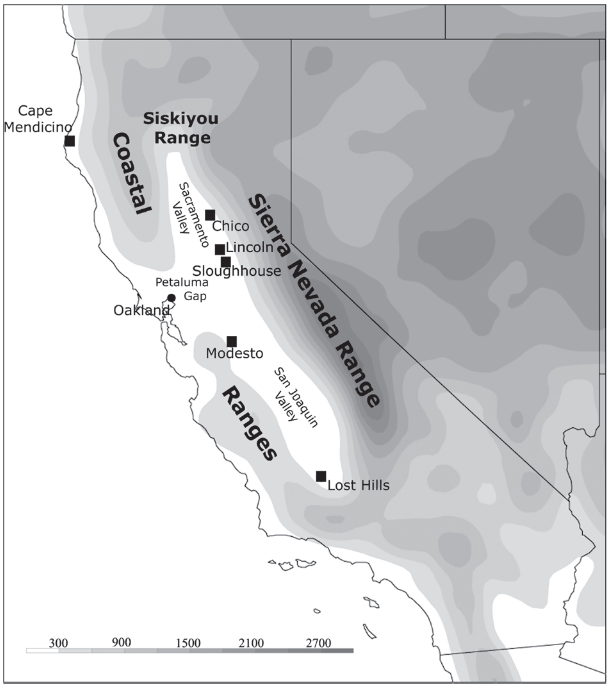

FIG. 1. WRF model terrain base map (m) showing the significant geographical locations referenced in the text, the GPS–IWV locations (square markers), and the Oakland rawinsonde sounding site (circle marker).

(Reeves and Lin 2008; Didlake 2007). Reeves and Lin (2008) described this case as having predominately zonal flow and a strong southerly barrier jet. They found that an isolated local maximum of precipitation in the vicinity of Plumas National Forest in the northern Sierra was associated with differential advection of incident airstreams yielding localized convergence. The 29–31 December 2005 storm caused major flooding along the Russian, Napa, and Truckee Rivers, several mudslides, and flooding in the streets of San Francisco and Reno (California–Nevada River Forecast Center).

2. Data

Atmospheric water vapor is regularly measured by several types of instruments. Over the ocean, the SSM/I aboard the Defense Meteorological Satellite Program (DMSP) polar-orbiting satellites are able to retrieve integrated water vapor (IWV) by measuring the thermal emission of both the earth's atmosphere and surface, and then relating them to the brightness temperature model function (Wentz 1997). Composite images from passes during the polar orbits of the SSM/I units are available roughly every 12 h. Over land, IWV is observed using near real-time GPS integrated precipitable water (IPW) receivers (Bevis et al. 1992). These point measurements of IWV (available every 15–30 min) are made possible with collocated measurements of temperature and pressure at over 200 sites across the United States. We equate SSM/I IWV over ocean with GPS IPW over land, and will use the term IWV hereafter. In this study, we use GPS IWV measurements from Cape Mendicino, Chico, Modesto, Lost Hills, Lincoln, and Sloughhouse, California, and vertically integrated water vapor computed from upper air soundings obtained in Oakland, California (Fig. 1). Even though the combination of these observations provides greater detail of the movement of water vapor over the globe than ever before, the current observing systems have several limitations, including coarse temporal sampling of about 12 h by the polar-orbiting satellites and a limited number of IWV measurements over land.

For verification of the wind and thermodynamic profiles, we compare model output to the Oakland upper-air soundings and to the time series of observed wind profiles from the 915 MHz (UHF) National Oceanic and Atmospheric Administration (NOAA) wind profiler located at Chico (Fig. 1; Ecklund et al. 1988; Weber et al. 1993).

3. Methodology

a. Drying ratio

As water vapor is forced to rise over a mountain barrier, the condensation of water vapor and the conversion to and fallout of precipitation will lead to decreased water vapor content downstream of the ridge. The amount of water vapor removed is related to the original amount by the ''drying ratio'' (Smith et al. 2005):

$$\text{Drying ratio} = \frac{\text{water vapor removed}}{\text{initial water vapor}}. \tag{1}$$

The drying ratio is a good parameter for evaluating water vapor depletion, or airmass transformation, since unlike precipitation efficiency, no knowledge of the vertical velocity of air is required. Calculations for different mountain ranges have found a spread of drying ratio values (Table 1), from 35% over the Alps (Smith et al. 2003) to 50% over the Andes (Smith and Evans 2007). Significant mountain ranges deplete, on average, at least one-third of the original water vapor of an impinging cross-barrier air mass. A more recent study by Didlake (2007) found an average drying ratio of around 30% over northern California, with a value as high as 66% for one individual storm based on comparisons of water vapor content from upper air soundings upstream (i.e., Oakland) and downstream of the Sierra Nevada

TABLE 1. Drying ratios from past studies for various mountain ranges; Alps (Smith et al. 2003), Andes (Smith and Evans 2007), and Oregon Cascades (Smith et al. 2005). The drying ratio for northern California includes both the Coastal Range and Sierra Nevada range and is an average of 15 cases presented in Didlake (2007).

Mountain range	Drying ratio (%)
Alps	35
Andes	50
Northern California	32
Oregon Cascades	43

range (i.e., Reno, Nevada). These previous papers estimate drying ratios using the cross-barrier wind and hence treat the depletion of water vapor over terrain as approximately two-dimensional.

b. Regional model design

Numerical model output is used to provide a more spatially and temporally continuous water vapor field and water vapor transport than is available from observations in our region of interest. We employ the Weather Research and Forecasting (WRF) model version 2.2 (Skamarock et al. 2005) to obtain high-resolution information on water vapor and its transport both over the ocean and land. This study utilizes the Advanced Research WRF (ARW) dynamical core, which is fully compressible, Euler nonhydrostatic, and uses terrain-following sigma (σ) coordinates. More information on the details of WRF ARW is available in Skamarock and Klemp (2008), Skamarock (2006), and others. The North American Regional Reanalysis (NARR) 32-km gridded reanalysis dataset (Mesinger et al. 2006) was used to initialize the model and update boundary conditions every 3 h.

One nested domain was used for the simulations (Fig. 2). Domain 1 used 27-km grid spacing with 150 $\times$ 130 grid points, and domain 2 used 9-km grid spacing with 241 $\times$ 196 grid points. Both domains used 30-s terrain resolution and 45 vertical levels distributed unevenly and maximized in the boundary layer. Time steps of 108 and 36 s were used for domains 1 and 2, respectively. In their study on the sensitivity of quantitative precipitation forecasting (QPF) skill of wintertime storms in the Sierra Nevada to microphysical parameterization and horizontal resolution, Grubišić et al. (2005) found that QPF skill scores were not improved by reducing the numerical grid size below 13.5 km. The atmospheric river associated with the targeted storm made landfall on the northern California coast early on 30 December. The model was initialized at 0000 UTC 29 December to allow for spin up. The simulations were run for 96 h, through 0000 UTC 2 January 2006. The Kain–Fritsch cumulus parameterization scheme, Thompson microphysical parameterization scheme, and the Mellor–Yamada–Janjic boundary layer and surface layer parameterization schemes were each used for both domains.

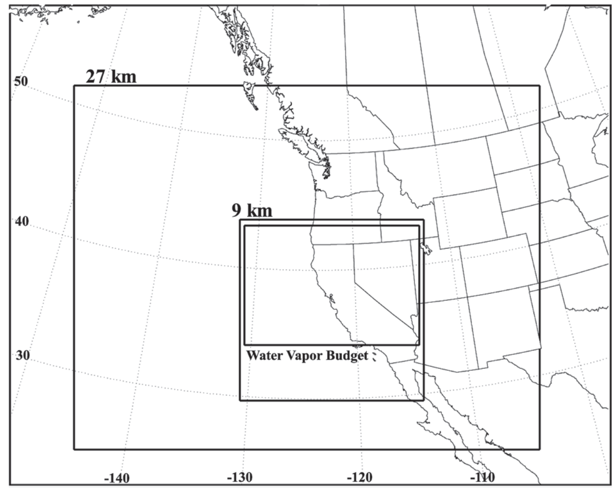

FIG. 2. WRF model domain set up for 27-km outer and 9-km inner domains, and the large-scale water budget domain within the inner model domain.

The transport of scalar quantities, in this case the mixing ratios of water vapor and hydrometeors, creates complications when considered in more than one dimension where negative mixing ratios are often set to zero (Braun 2006). This has significant implications near large moisture gradients and can lead to errors in the evaluation of water vapor transport from 3D model output. Version 2.2 of the WRF model was updated to include a positive-definite moisture transport scheme (PDMTS; Skamarock 2006), which is critical to the closing of the water budget of the WRF model (Skamarock and Weisman 2009; Hahn and Mass 2009; Lin and Colle 2009, manuscript submitted to *Mon. Wea. Rev.*). Initial simulations were run with WRF version 2.1.2, which yielded a large discrepancy between total precipitation and water vapor convergence. Although differences in model fields at individual times between runs with and without a PDMTS were typically small and difficult to notice, these small differences at each model time step became significant over the duration of the run and were a major factor in the water budget closure.

Two sensitivity tests were performed, with the same initial conditions and model design as the control run (CTRL; Fig. 3a). The sensitivity tests isolate the effects of the terrain on blocking water vapor transport by removing just the Coastal Range north of Oakland (NOCR run, Fig. 3b), and removing all terrain within the domain (NOTER run, not shown). By removing all of the mountains, the impact of the entire West Coast

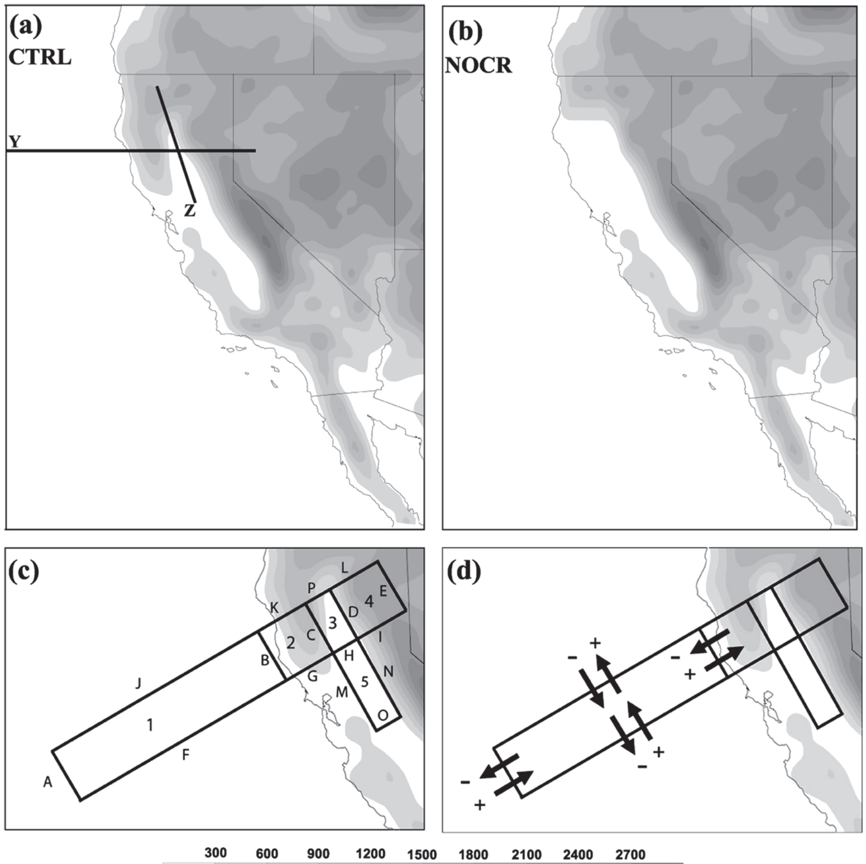

FIG. 3. WRF model terrain elevation (shaded, in m) for (a) CTRL, (b) NOCR runs (each labeled), and cross-section reference lines labeled Y and Z. (c) Layout of small-scale water budget boxes with sides labeled A–P and boxes labeled 1–5, and (d) the assignment of positive and negative flux values used in the water vapor flux analysis of box sides (the same convention applies to each box side) Note: sign conventions in (d) are not the same as those used in the water budget.

mountain complex on inland water vapor transport can be examined. Land use remained the same for all three simulations (CTRL, NOCR, and NOTER). In the NOCR run, all the terrain height values were set to 0 for the section of the northern Coastal Range that we wanted to remove. North of the range, terrain height and slope values were systematically increased (in a steplike manner) so that the model terrain had the profile of a quickly rising slope. For NOTER, all the height values of terrain were set to 0.

c. *Integrated water vapor*

It is critical that the model be able to represent the magnitude, as well as the timing of the increase and decrease of IWV associated with the atmospheric river. The model produces water vapor mixing ratios for each model level, which are then used to compute IWV (mm) for each two dimensional horizontal grid box by the expression:

$$\mathrm{IWV} = \frac{1000}{\rho_w g} \int q_v \, dp, \tag{2}$$

where g (m s^{-2}) is the gravitational acceleration, ρ_w is the density of water (1000 kg m^{-3}), q_v (kg$_{\mathrm{water}}$ kg$_{\mathrm{air}}^{-1}$) is the layer average water vapor mixing ratio between each model level, and dp (Pa) is the depth between each model level over which q_v is computed.

d. *Horizontal water vapor flux*

The vertically integrated horizontal water vapor flux (kg m^{-1} s^{-1}) at each grid point along a box side is computed with positive and negative flux values assigned following the arrows in Fig. 3d, using

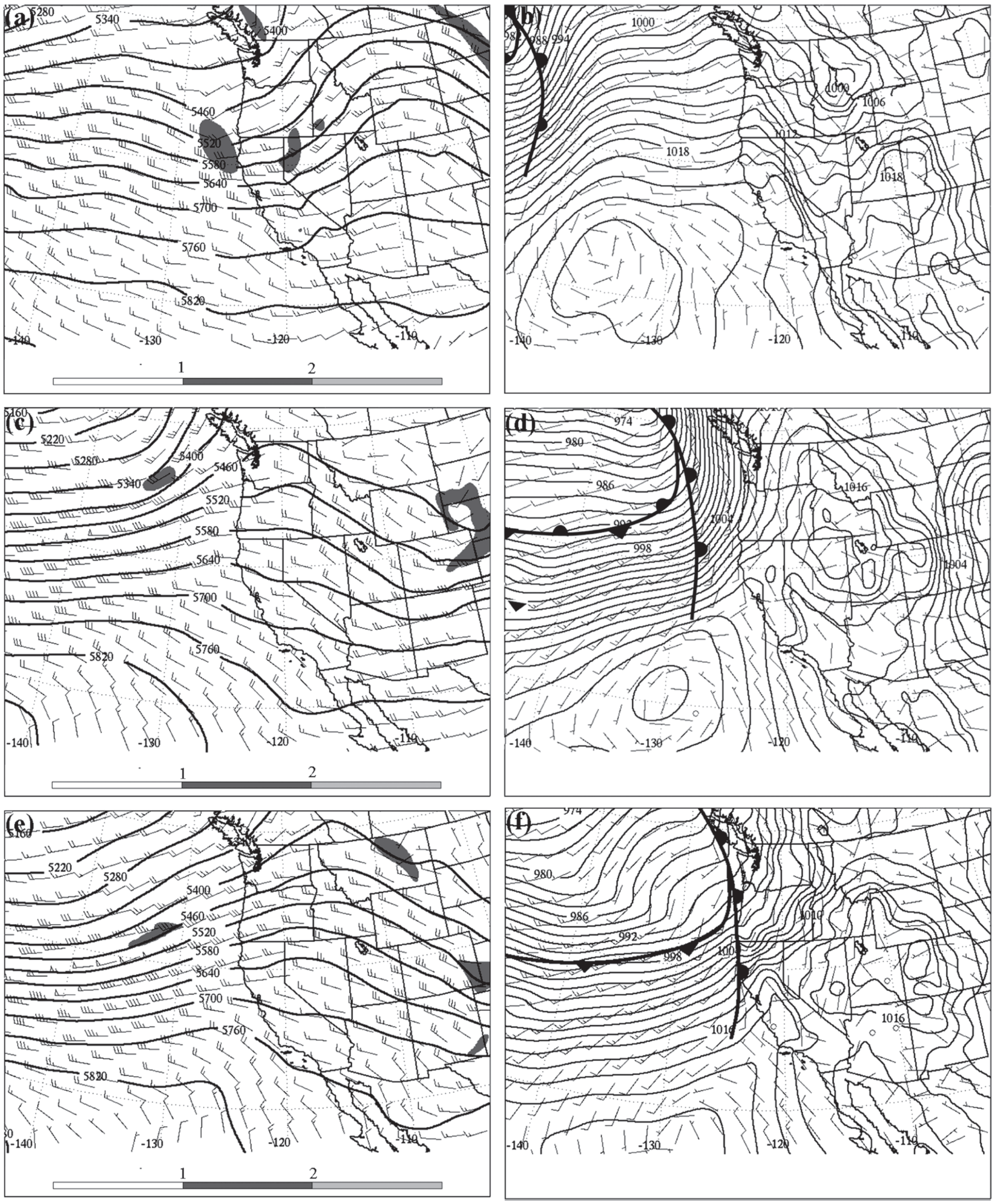

FIG. 4. NARR 500-hPa geopotential height (contours, m), vorticity (shaded, 10^4 s^{-1}), and wind (barbs, m s^{-1}) at (a) 0000 UTC 29 Dec, (c) 0000 UTC 30 Dec, and (e) 1200 UTC 30 Dec 2005. NARR sea level pressure (contours, hPa), 10-m wind (barbs, m s^{-1}), and surface fronts at (b) 0000 UTC 29 Dec, (d) 0000 UTC 30 Dec, and (f) 1200 UTC 30 Dec 2005.

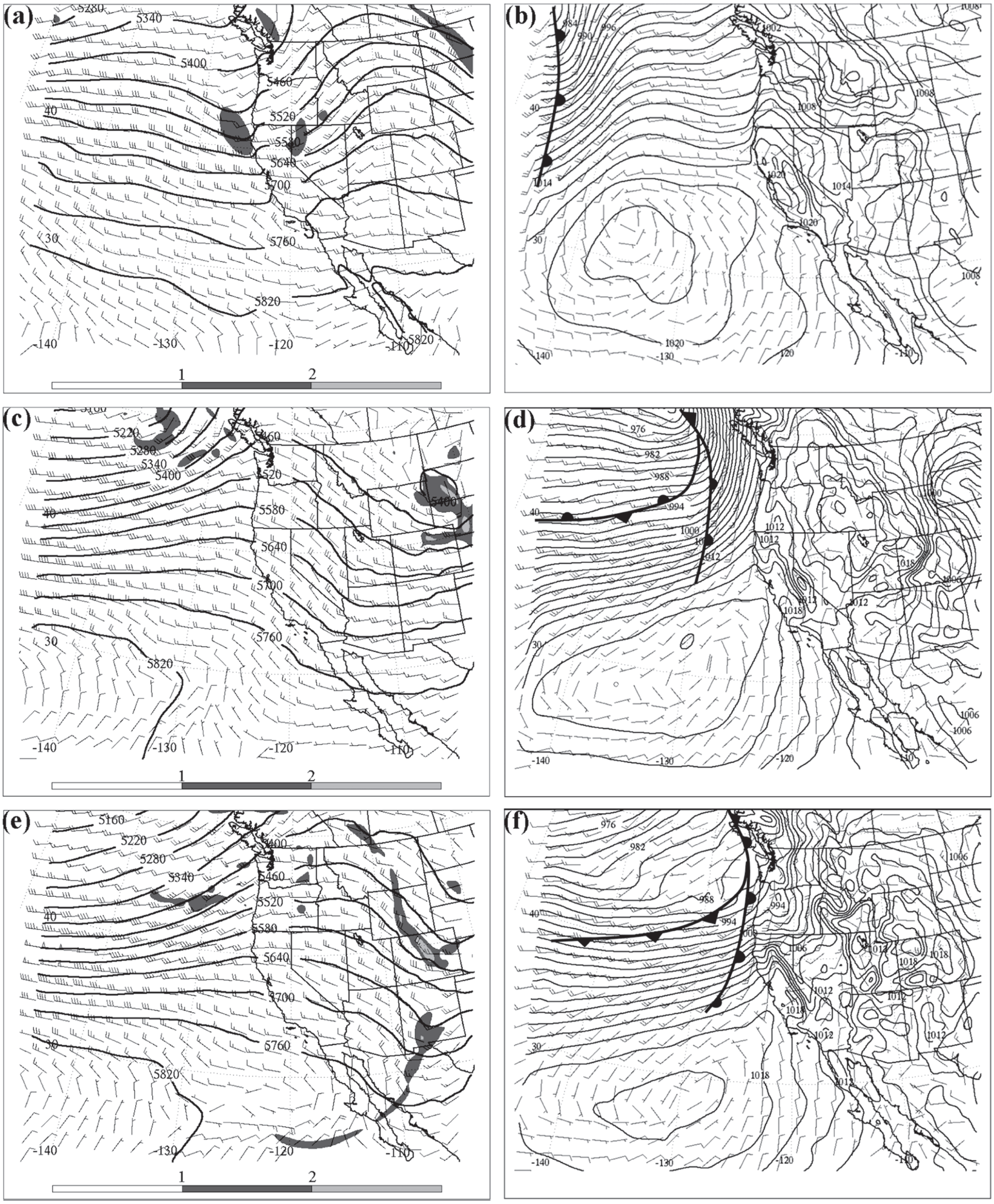

FIG. 5. WRF CTRL run 500-hPa geopotential heights (contours, m), vorticity (shaded, $10^4\ s^{-1}$), and wind (barbs, m s^{-1}) at (a) 0000 UTC 29 Dec, (c) 0000 UTC 30 Dec, and (e) 1200 UTC 30 Dec 2005. WRF CTRL run sea level pressure (contours, hPa), 10-m winds (barbs, m s^{-1}), and surface fronts at (b) 0000 UTC 29 Dec, (d) 0000 UTC 30 Dec, and (f) 1200 UTC 30 Dec 2005.

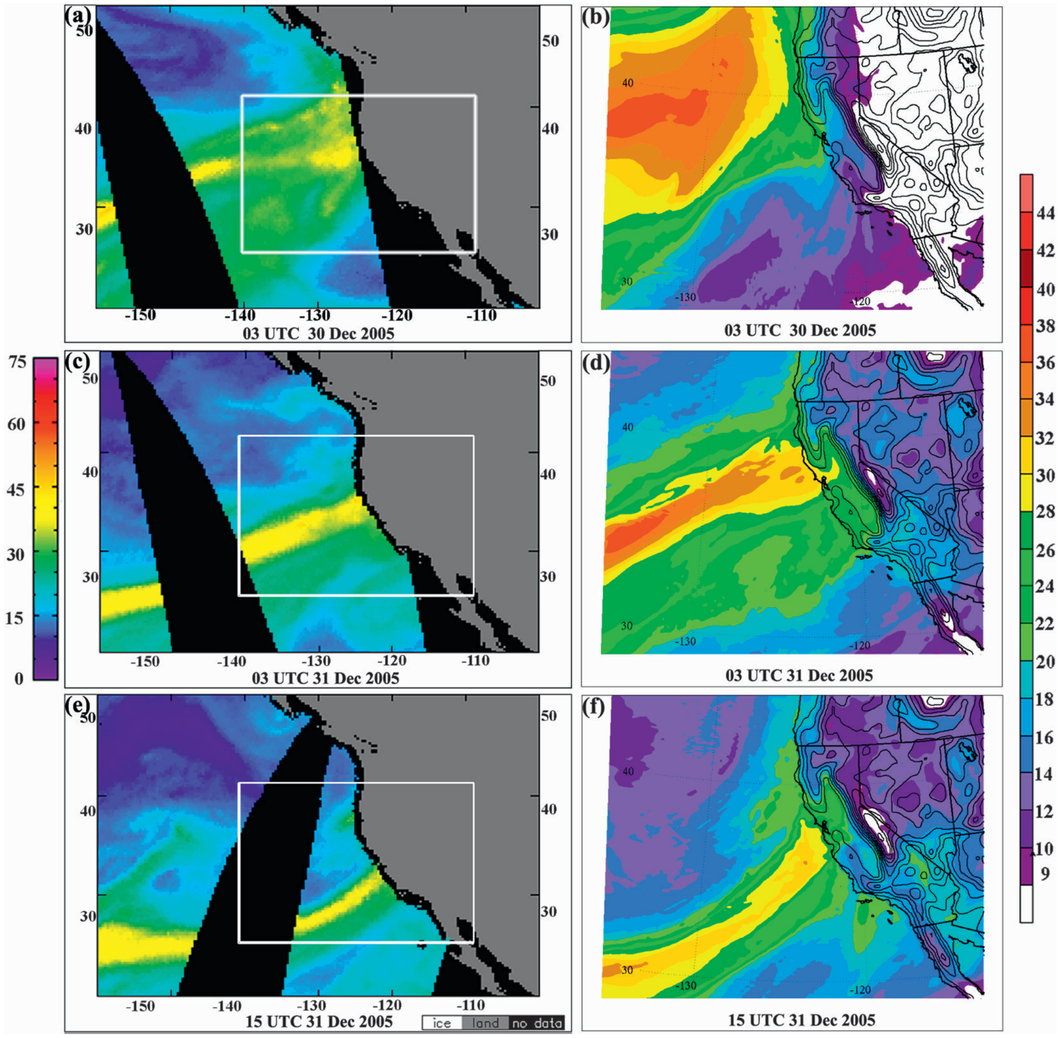

FIG. 6. SSM/I passes of IWV (mm) from approximately (a) 0300 UTC 30 Dec, (c) 0300 UTC 31 Dec, and (e) 1500 UTC 31 Dec 2005. Times of passes are labeled above and below each satellite coverage swath. Dark regions are areas not covered by ascending and descending satellite passes. Corresponding WRF-simulated IWV (mm) from CTRL run inner domain [cf. white outline in (a),(c),(e)] for (b) 0300 UTC 30 Dec, (d) 0300 UTC 31 Dec, and (e) 1500 UTC 31 Dec 2005. (Note: color scales do not match perfectly. Source: Remote Sensing Systems SSM/I data.)

$$Q_{\mathrm{Flux}} = \frac{1}{g}\int q_v V_n \, dp, \tag{3}$$

where g, q_v, and dp are defined as in Eq. (2), and V_n is the layer average horizontal wind (m s^{-1}) normal to a budget box side over dp. The flux of all other hydrometeor species, defined as q_t, including ice, cloud water, cloud ice, graupel, snow, and rain, is computed using the same method and substituting q_t for q_v in (3). The water vapor flux is computed every 15 min and the instantaneous values are assumed to be constant during the 15 min.

e. Water budgets

A regional-scale water budget is computed for a region approximately two-thirds the size of the model 9-km inner domain (Fig. 2) to test the horizontal water vapor flux computation with the model total water fields. The conservation equation for water substance

$$\frac{\partial S}{\partial t} = F + E - P \tag{4}$$

is evaluated using a 15-min time step, where S is the storage of water in the atmosphere as water vapor and other hydrometeors, F is the flux convergence of water fields through the sides of the volume, E is evaporation from the surface, and P is the precipitation fallout within the budget box. Here, all terms on the right-hand side of (4) are expressed in millimeters (15 min)$^{-1}$ (which is equivalent to the units of mass flux kg m^{-2} s^{-1}) to

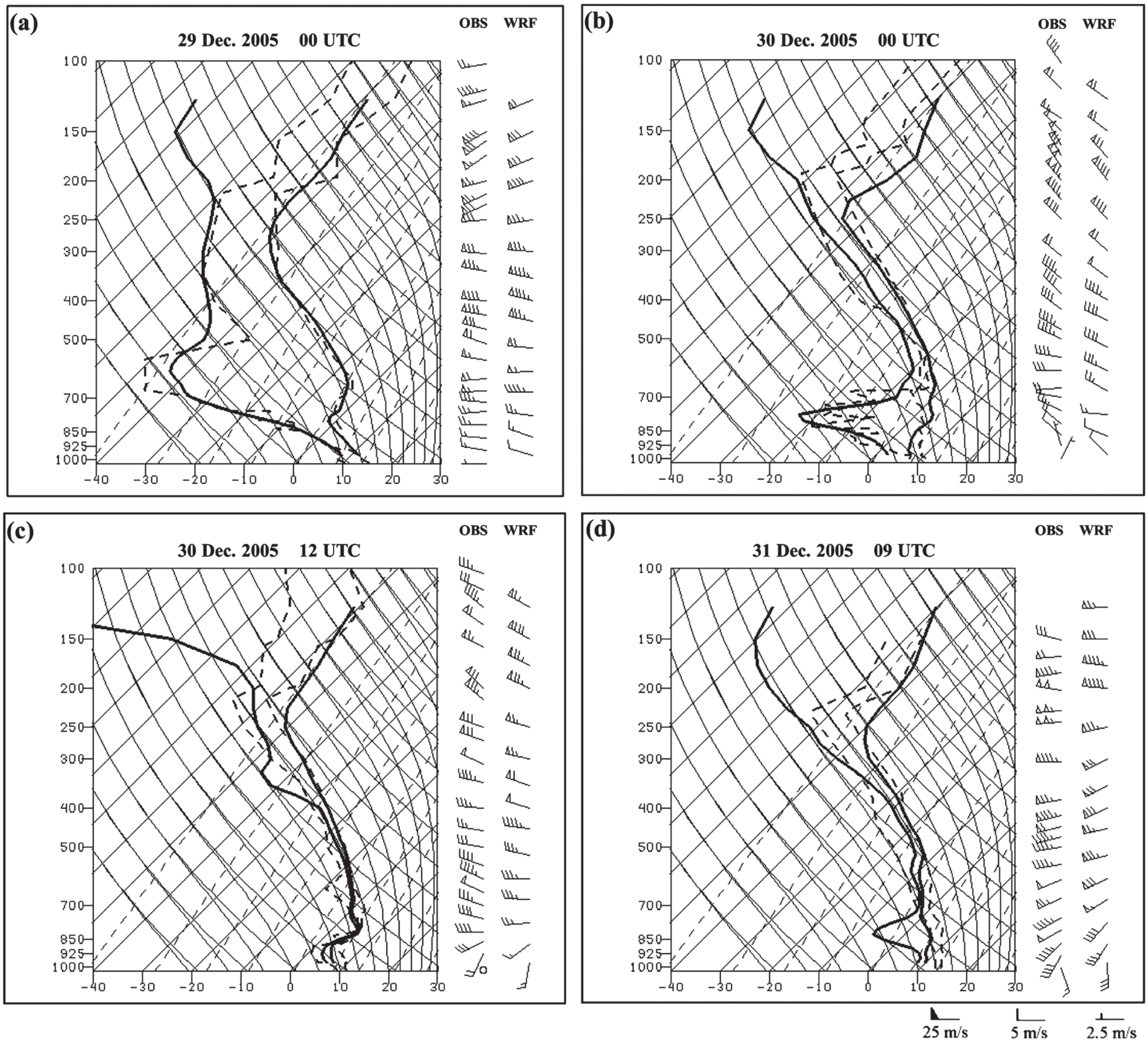

FIG. 7. Skew *T*–log*p* plots of observed (solid curves) and simulated (dashed curves) upper-air soundings from Oakland, CA at (a) 0000 UTC 29 Dec, (b) 0000 UTC 30 Dec, (c) 1200 UTC 30 Dec, and (d) 0900 UTC 31 Dec 2005. The left wind profile is observed and the right wind profile is simulated. Wind barbs in m s^{-1} with a legend at the bottom right.

facilitate comparisons to IWV measurements. The computations of each term are described below.

There are two main components of the total water substance flux convergence in this budget; the vertically integrated horizontal water substance flux in (3) and the surface water vapor flux. The contribution due to the vertically integrated horizontal water substance flux within a defined area can be computed using the line integral around the budget area:

$$F_{\text{horiz}} = \frac{\rho_w}{A} \oint Q_{\text{Flux}}\, dl, \tag{5}$$

where A is the area of the box (m^2), ρ_w is the density of water (1000 kg m^{-3}), Q_{Flux} is defined in (3) and converted to a 15-min flux (kg m^{-1} 15 min^{-1}), and dl is the length of a box side (m). The horizontal winds used in (5) are normal to the box sides. Flux into the box on the lateral sides is defined to be positive flux. It is assumed that no water vapor or other hydrometeors exit through the top of the box, a reasonable assumption since the top of the box is at 100 hPa.

The surface water vapor flux F_{sfc} is directly output from the model in units of millimeters (15 min)$^{-1}$. Positive surface water vapor flux is defined as upward, or into

TABLE 2. Integrated water vapor (mm) obtained from the Oakland upper-air soundings compared to the model output at the same times and location.

	Oakland	
Time and date	Obs	Model
0000 UTC 29 Dec	12.85	11.47
1200 UTC 29 Dec	13.94	12.17
0000 UTC 30 Dec	18.24	17.22
1200 UTC 30 Dec	27.2	26.6
1500 UTC 30 Dec	24.7	28.29
1800 UTC 30 Dec	27.36	28.33
2100 UTC 30 Dec	29.16	29.64
0000 UTC 31 Dec	29.44	30.12
0300 UTC 31 Dec	31.58	30.57
0600 UTC 31 Dec	30.69	30.1
0900 UTC 31 Dec	29.56	29.14
1200 UTC 31 Dec	30.73	28.67

the box. Precipitation from the model output is a storm accumulated total. The change in storm accumulated precipitation at every output time yields a rain rate in [mm (15 min)$^{-1}$]. Surface evaporation E and evaporation due to microphysics are not explicitly computed in this study and can be accounted for in the storage term S.

Water budgets were also computed for five boxes placed in locations that would capture water vapor flux offshore, along the coast, and inland to diagnose airmass transformation over the key areas (Fig. 3c). Calculations for these smaller boxes were performed using the same mathematical methodology described above. To capture the effects of the mountain range, the box sides were oriented orthogonal and parallel to the main axis of the Sierra Nevada range, which was approximated to be 26°W of north. The terrain parallel box sides are also perpendicular to the along-flow axis of the atmospheric river (Fig. 3c; labels A–E, M, N). The other nine sides closed the boxes to complete the water budget on its lateral sides, with sides H and P designed to measure the amount of water vapor entering the valley from the south and exiting the valley to the north, respectively. No single set of small boxes can perfectly capture the water vapor fluxes during the storm since it takes finite amount of time for water vapor to traverse a box and in that time the axis of the atmospheric river can shift out of the box. These small boxes are designed to capture the majority of the fluxes for representative areas. As a result, we expect that the small box budgets will not balance as closely as the regional-scale budget.

4. Storm description and model verification

a. *Synoptic flow and atmospheric river*

The large-scale flow during the 29–31 December 2005 storm was characterized by a long-wave 500-hPa trough over the Pacific Ocean (Figs. 4a,c,e), with an occluding surface cyclone in the Gulf of Alaska (Fig. 4b). At 0000 UTC 30 December, a surface front and low pressure trough extended from the Washington and Oregon coasts to the southwest into the central Pacific (Fig. 4d). Initially, the surface cold front moved eastward as water vapor in the atmospheric river surged northeastward in the warm sector (Figs. 4a,b). The WRF model was able to simulate the overall development and movement of the storm system. The modeled upper-level (Figs. 5a,c,e) and surface flow (Figs. 5b,d,f) compared well to the observed flow (Fig. 4), although the modeled warm front's position lagged the observations by about 4 h. SSM/I imagery from the morning of 30 December (Fig. 6a) revealed a broad, ill-defined area of enhanced IWV off the West Coast, with remnant enhanced IWV extending northwestward into the Gulf of Alaska near the main low pressure center (not shown). As the cold front began to advance southward (Fig. 4f), local moisture convergence within the warm conveyor belt (Bao et al. 2006) focused the broad area of IWV into a narrow and well-defined atmospheric river by 0300 UTC 31 December (Fig. 6c). The atmospheric river was directed southwest to northeast, toward the California coast. A comparison of the SSM/I imagery of IWV with model simulated IWV shows that the initialization and simulation of the water vapor field was also representative (Fig. 6). The atmospheric river simulated by the model was remarkably similar to the observed river, with core IWV values within a few millimeters of the observed values. The simulation also represents the evolution of the water vapor from a broad plume to a narrow, focused river of water vapor (Fig. 6).

Along the coast at Oakland, the air mass was initially dry (Fig. 7a), but as the atmospheric river approached, water vapor along the warm front caused gradual moistening, first at midlevels near 700 hPa (Fig. 7b), then later at 850 hPa (Fig. 7c). It was during the passage of the warm front and atmospheric river, aided by the prefrontal LLJ (Fig. 7d), that the heaviest precipitation transitioned from along the Coastal Range to the windward slopes of the Sierras, with some locations along the windward slopes of the Coastal Range receiving over 150 mm of precipitation in a 24-h period. As the system moved to the east and made landfall, the cold front began to advance southward (evident in a limited number of observations over the open ocean; not shown) and enhanced the water vapor gradient across the atmospheric river, causing the river to narrow (Figs. 6c,e). The cold front and IWV continued to move south down the California coast on 31 December, causing a shift in the heaviest precipitation totals from the north to south along the Sierras (not shown) on

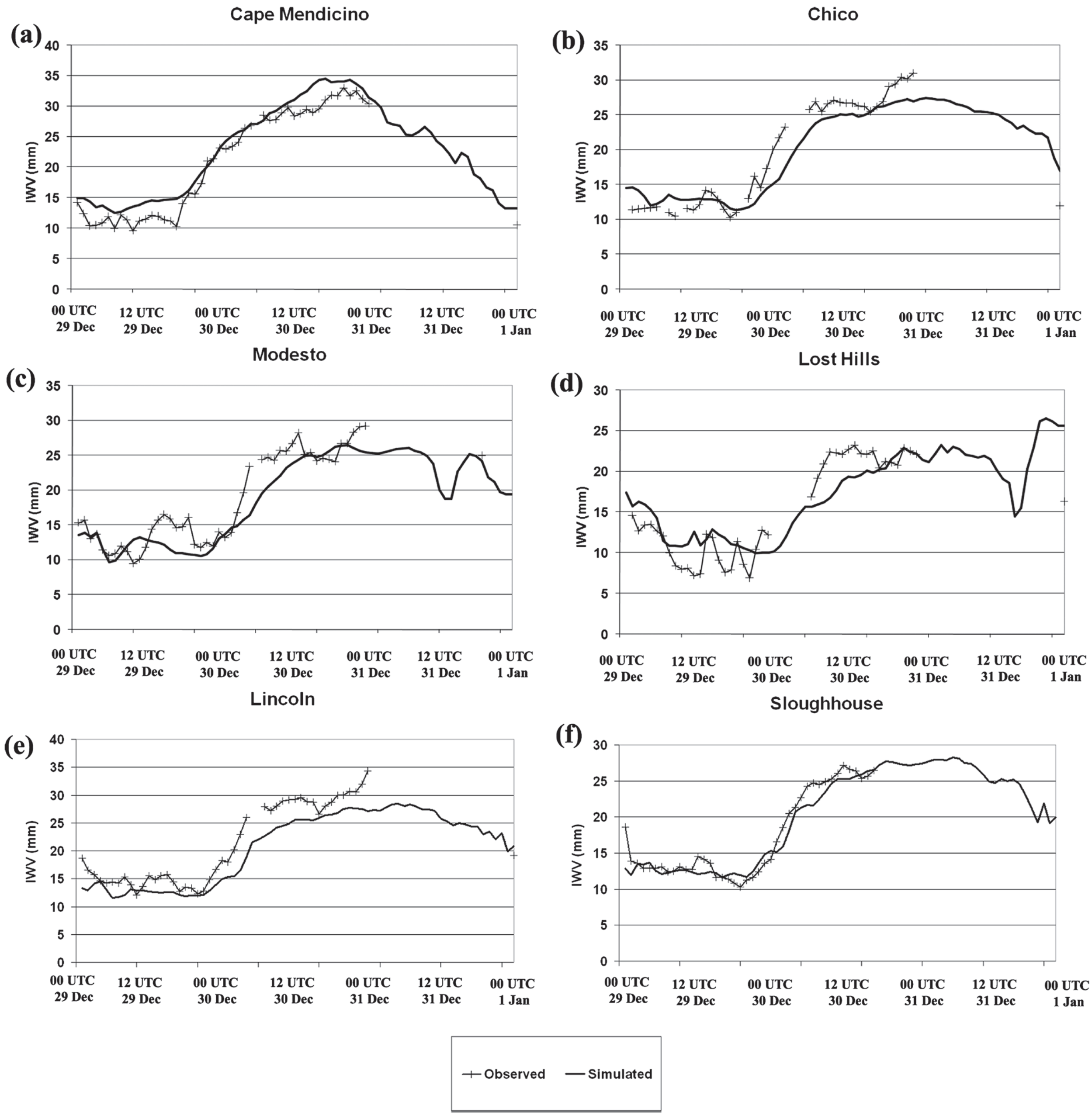

FIG. 8. Comparison of GPS IWV (mm) values (cross-hatched lines) and WRF CTRL run simulated IWV values (solid lines in mm) from 0000 UTC 29 Dec 2005 to 0000 UTC 1 Jan 2006 at (a) Cape Mendicino, (b) Chico, (c) Modesto, (d) Lost Hills, (e) Lincoln, and (f) Sloughhouse. None of the GPS–IWV stations reported data for the entire period.

1 January 2006. At Oakland, the wind profiles are reasonably well simulated but the moisture and temperature profiles differ between the observations and model output. Despite the differences in the moisture profiles, the simulated vertically integrated moisture (Table 2) is either lower or within 1 mm of the observed values. In later sections, we will make a case that the northward flux of moisture along the base of the Sierras is significant. Underestimation of simulated moisture at Oakland weakens but does not negate our results.

Since SSM/I imaging techniques are only valid over the ocean, point values of GPS–IWV data are used to verify the time series of IWV as the storm passes. Figure 8 show that the observed and model simulated IWV agree very well. The model was able to represent the increase and decrease of IWV, as well as the relative magnitudes of IWV associated with the air masses at each location.

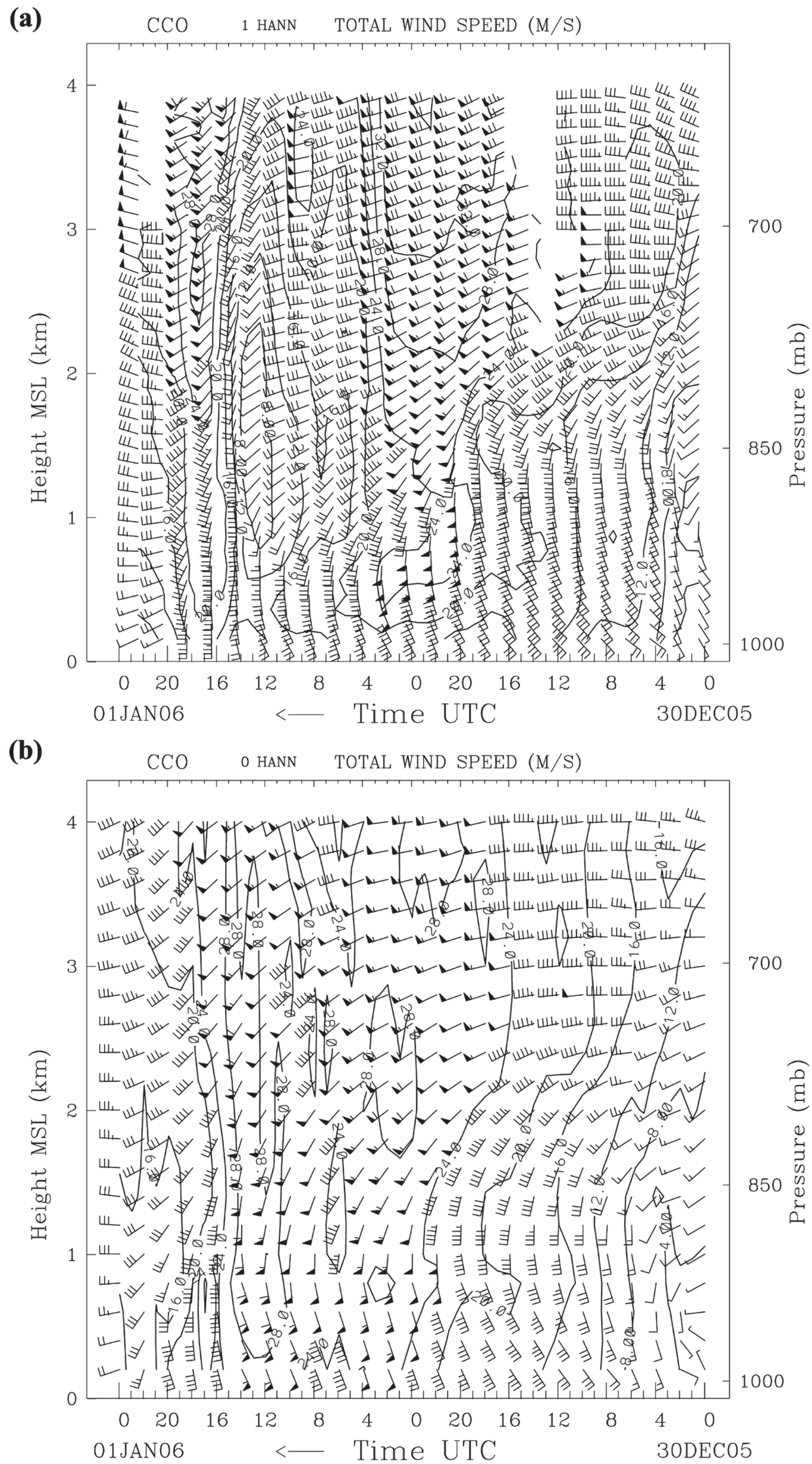

FIG. 9. Wind profiles below 4 km (barbs and contoured) for 30–31 Dec 2005 from (a) Chico (CCO) wind profiler and (b) WRF CTRL simulation. Wind barbs are in m s^{-1}, with time reading from right to left.

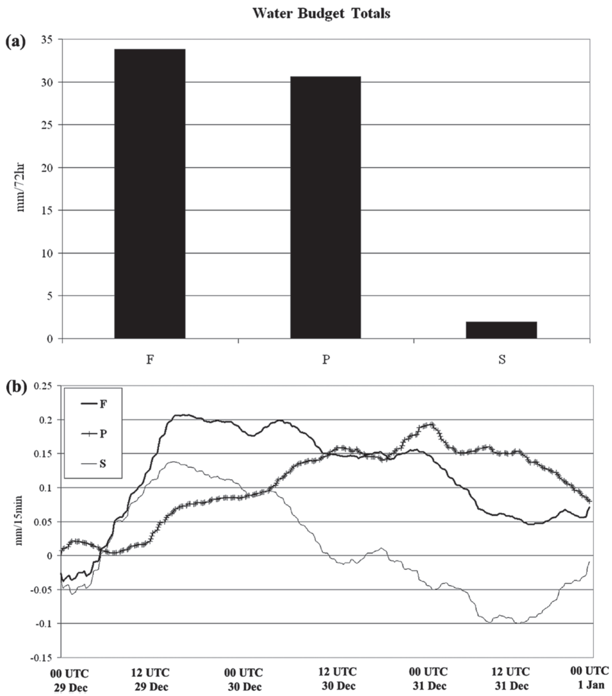

FIG. 10. Large-scale water budget showing water substance flux convergence, precipitation, and storage for the WRF CTRL run: (a) 72-h totals [mm (72 h)$^{-1}$], and (b) 15-min rates [mm (15 min)$^{-1}$].

Some GPS–IWV data were not available on 31 December, but the model results show a steady decline of IWV as the system passes.

b. The barrier jet

An airstream approaching a mountain barrier will be blocked rather than rising easily over terrain when the Froude number is <1 (Fr = U/Nh; where U is the barrier-normal wind speed, N is the Brunt–Väisälä frequency, and h is the barrier height; e.g., Pierrehumbert and Wyman 1985; Smolarkiewicz and Rotunno 1990). The blocked flow is present upstream and below the top of the mountain barrier and is deflected leftward in the Northern Hemisphere by the Coriolis force. The low-level blocked flow often contains a barrier jet paralleling the long axis of the high terrain and maintained by a statically stable pressure ridge dammed against the windward slope. Barrier jet flows have been associated with mountain ranges across the world and can locally redistribute precipitation.

Based on data from the Chico wind profiler, the low-level flow in the Sacramento Valley was southeasterly at 0000 UTC 30 December (Fig. 9a), and strengthened to up to a maximum of 25 m s^{-1}. The barrier jet was strongest at 0.5-km altitude between 20 UTC 30 December and 0200 UTC 31 December and contributed to the northward transport of water vapor within the Sacramento Valley. The timing of the barrier jet maximum and the landfall of the relatively higher IWV values roughly coincide.

The barrier jet that developed along the windward slope of the Sierras within the Sacramento Valley is also represented in the WRF simulation (Fig. 9b). The low-level winds turn to southeasterly after 0200 UTC 30 December and wind speeds ≥25 m s^{-1} persist from 0000 to 1400 UTC 31 December. In the model, the strongest winds within the barrier jet extend to lower altitudes and the peak winds are slightly more intense (maximum 29 m s^{-1}) compared to the observations.

c. Regional-scale water budget

The regional-scale water budget (Fig. 10a) indicates an approximate closure of the horizontal water substance fluxes within the water vapor budget box shown in Fig. 2. The total precipitation is slightly less than the total water vapor convergence (Fig. 10a). The total convergence of

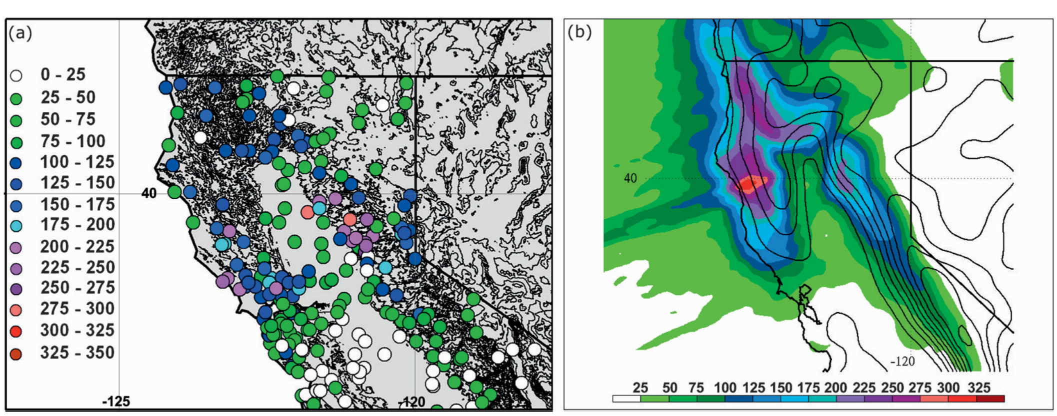

FIG. 11. The 72-h precipitation totals (mm) from (a) NWS COOP and (b) WRF CTRL run.

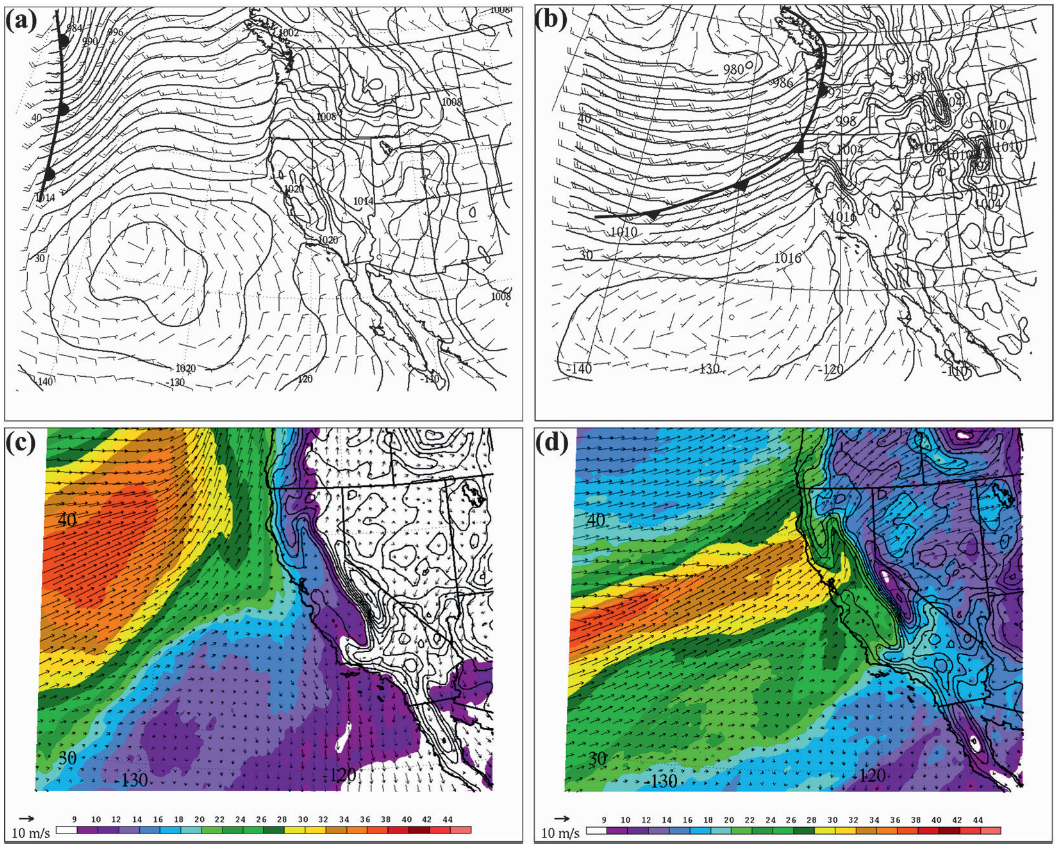

FIG. 12. Plots from the WRF CTRL run: sea level pressure (contours, hPa) and 10-m winds (barbs, m s^{-1}) with surface fronts for (a) 0000 UTC 30 Dec and (b) 0000 UTC 31 Dec 2005. IWV (color shaded, mm) and σ = 0.9205 winds (arrows, m s^{-1}) for (c) 0000 UTC 30 Dec and (d) 0000 UTC 31 Dec 2005.

water fields is dominated by the q_v flux convergence. The q_t flux out of the box is nearly negligible, likely attributable to the production and fallout of hydrometeors almost completely within the box. The storage of atmospheric water, or the water added during the 72-h run, is less than 10%. Examination of the IWV field near the end of the simulation indicates that much of the residual water vapor is located within the Sacramento Valley (not shown). The evolution of the flux convergence and precipitation fall out (Fig. 10b) reveals a strong convergence of water vapor early in the model run, with about a 6-h time lag before precipitation rates begin to increase.

d. Precipitation

Precipitation is often difficult to measure in complex terrain, because of difficulties in instrument siting, maintenance, and representativeness issues (Strangeways 1996). Compared to the National Weather Service Cooperative Observer Network (COOP) rain gauges (Fig. 11a), the storm total precipitation from the CTRL run (Fig. 11b) overestimated the precipitation in the Siskiyou Range, underestimated the amount of precipitation over the northern portion of the Sierra and misplaced the local maximum on the Sierra windward slope too far north. The model produced an anomalous local maximum of precipitation along the Coastal Range near 40°N, 124°W associated with a precipitating feature moving west-southwest over the ocean and then passing over terrain (see precipitation accumulation trace extending past 130°W in Fig. 11b). Simulations with different microphysics all produced the small bull's-eye of precipitation so it is likely related to orographic enhancement of a persistent frontal rainband. The observed pattern of surface precipitation is sensitive to the location of small-scale ridges and valleys that are unresolved at 9 km (Anders et al. 2006, 2007; Minder et al. 2008). Our confidence in the model's representation of the water substance fields rests on the approximate closure of the large scale water vapor budget (section 4c) and the model's ability to reproduce the evolution and amplitude of the observed water vapor field at the GPS IWV locations on both the Pacific coast and in the Central Valley (section 4a).

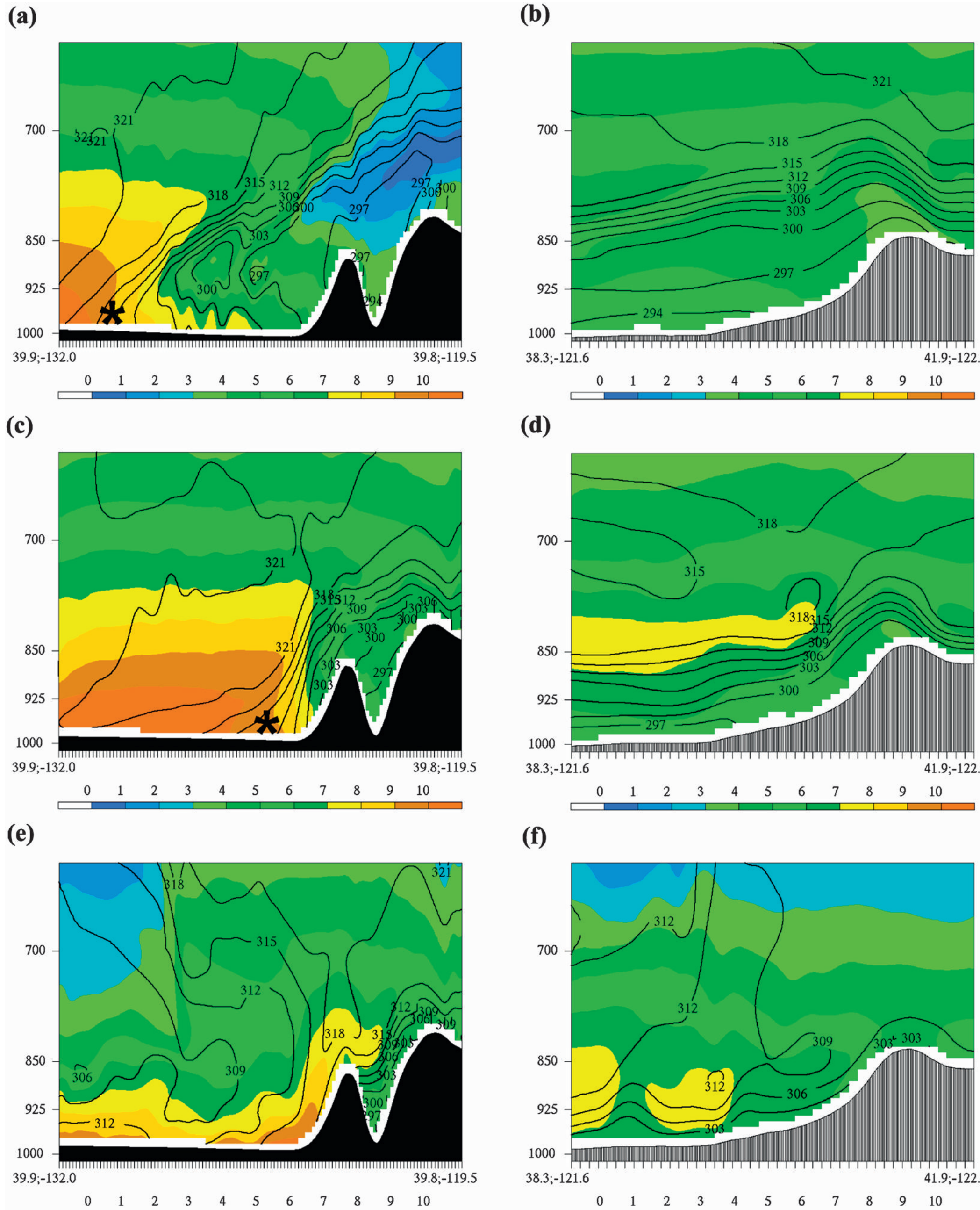

FIG. 13. CTRL WRF cross sections (pressure levels, hPa, labeled on left vertical axis) of equivalent potential temperature (contours, K) and water vapor mixing ratio (color shaded, g kg^{-1}): for cross-section Y (see Fig. 3) at (a) 0000 UTC 30 Dec, (c) 1200 UTC 30 Dec, and (e) 0000 UTC 31 Dec 2005; for cross-section Z at (also see Fig. 3) (b) 1200 UTC 30 Dec, (d) 0000 UTC 31 Dec, and (f) 1800 UTC 31 Dec 2005. Surface warm front position denoted by a star in (a) and (c).

5. Comparisons among sensitivity runs

a. Control run: CTRL

Early in the CTRL simulation, strong southwesterly low-level flow is evident between the approaching storm system and an anticyclone anchored off the southern California coast (Figs. 12a,b). At 0000 UTC 30 December, the atmospheric river is broad and fans out at the warm front (Fig. 12c). The low-level winds are blocked, which enhances the wind shift at the warm front and helps to keep the low-level water vapor offshore. Some of the offshore water vapor is lifted up

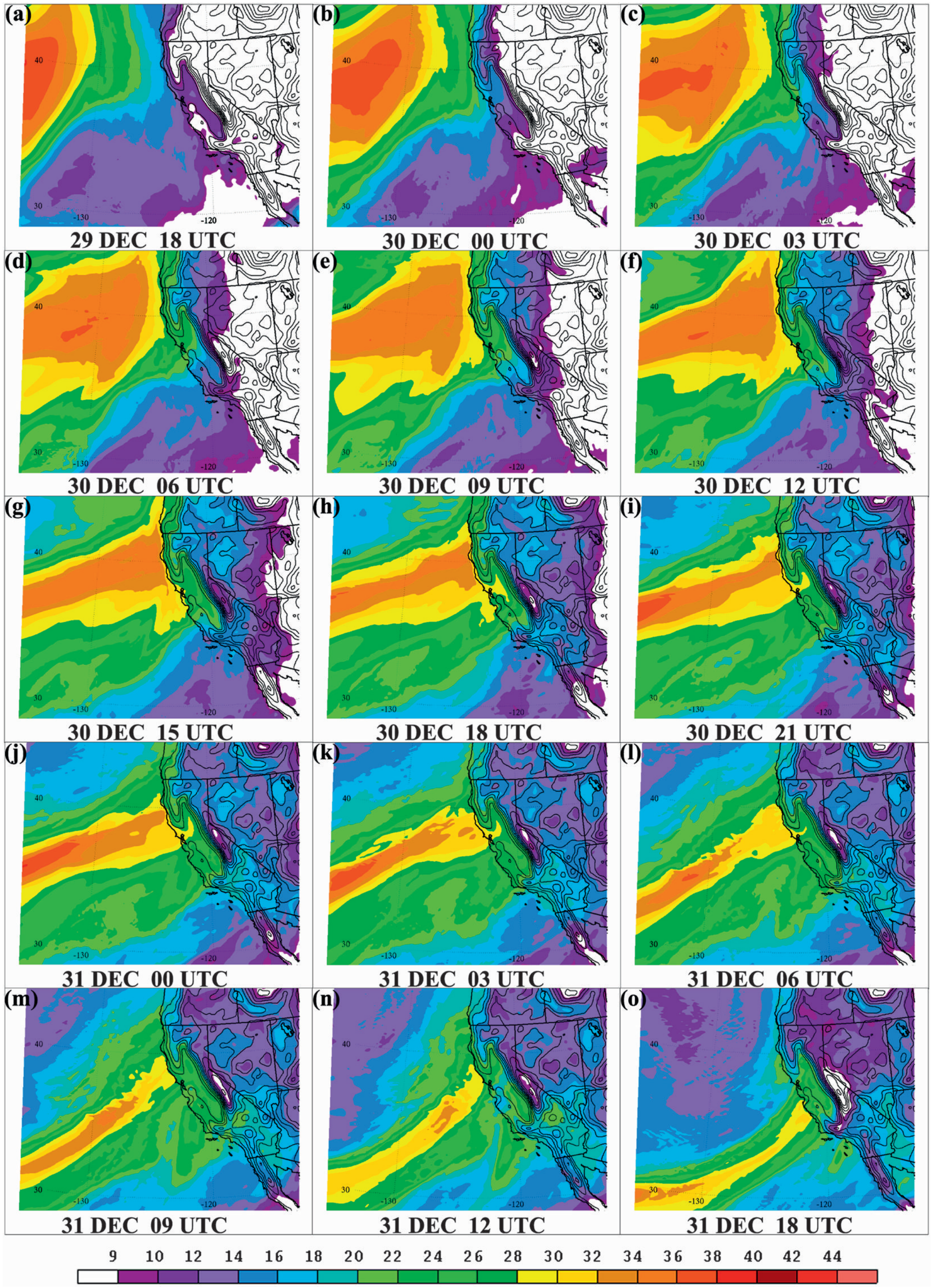

FIG. 14. WRF CTRL run IWV (color shaded, mm) at (a) 1800 UTC 29 Dec, (b)–(n) from 0000 UTC 30 Dec to 1200 UTC 31 Dec at 3-hourly intervals, and (o) 1800 UTC 31 Dec 2005.

and over the warm front (Fig. 13a). By 1200 UTC, the low-level water vapor impinges on the coast (Fig. 13c), and by 0000 UTC 31 December, the low-level winds (Fig. 12d) and some of the water vapor are able to ascend and cross the Coastal Range (Fig. 13e). The water vapor crossing the Coastal Range can first be seen in the Sacramento Valley as an elevated region of water vapor (Fig. 13d) that does not reach the surface. At 1800 UTC

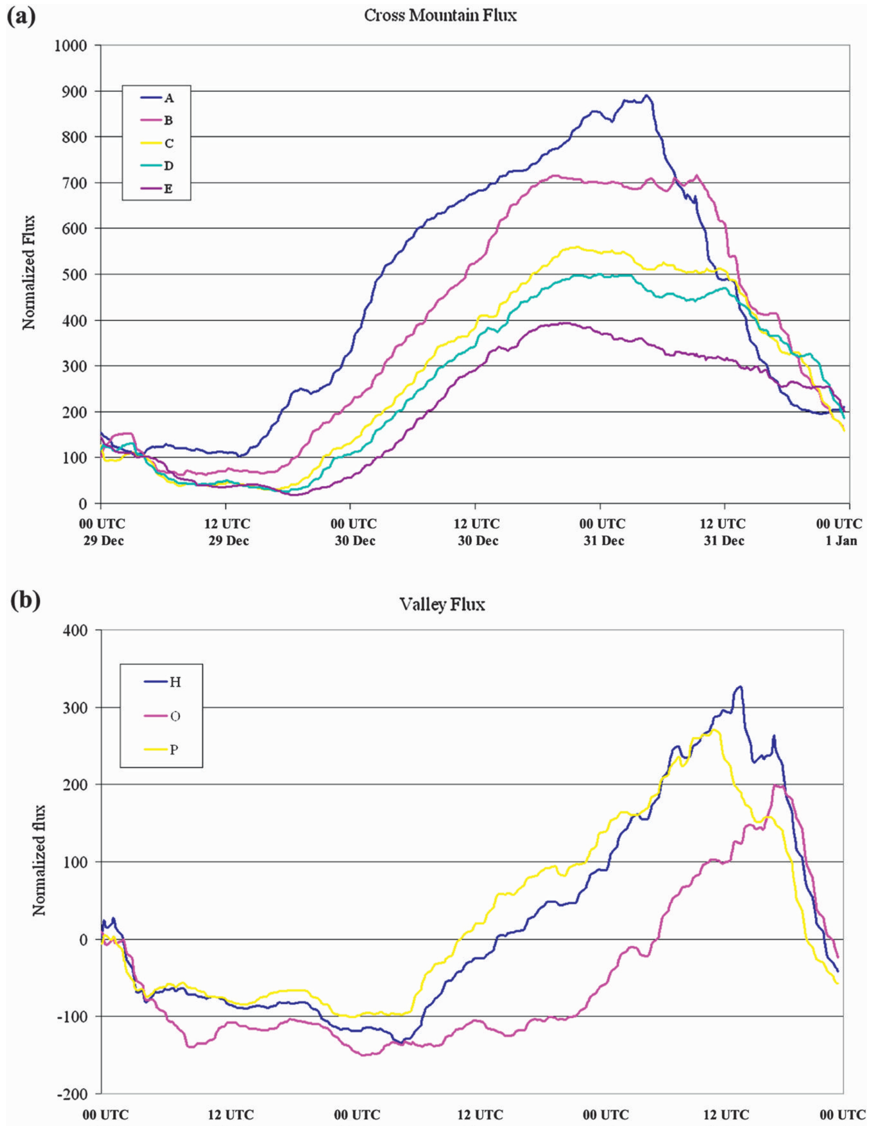

FIG. 15. WRF CTRL time series of normalized water vapor flux through sides (a) A–E (cross mountain flux), and (b) H, O, and P (valley flux). Flux values in kg m^{-1} s^{-1} and are normalized by the horizontal length (in m) of grid sides.

31 December, a low-level layer of higher mixing ratios advances up the Sacramento Valley (Fig. 13f). Eventually, the atmospheric river narrows and is pushed south by the advancing cold front.

1) Evolution of water vapor fluxes

Figure 14 summarizes the progression of the modeled atmospheric river. The atmospheric river first approaches the West Coast as a broad area of enhanced water vapor (Figs. 14a–d), and first impinges on the coastal terrain at 0900 UTC 30 December (Fig. 14e). The higher water vapor content air penetrates the Petaluma Gap at 1200 UTC 30 December (Fig. 14f), with the peak occurring around 0000 UTC 31 December (Fig. 14j). The atmospheric river continues to narrow and completely passes the Petaluma Gap by 1800 UTC 31 December (Fig. 14o).

The advection of water vapor associated with the atmospheric river in terms of fluxes offshore, near the coast, and within the Sacramento Valley is described by a time series of the water vapor flux results for sides A–E (see Fig. 4 for reference) in (Fig. 15a). The approach of the atmospheric river is evident in the rise in water vapor flux through the offshore sides (A and B), which peaks around 0000 UTC 31 December. A small reduction

TABLE 3. Summary of drying ratios for the CTRL, NOCR, and NOTER runs for box side A and the subsequent downstream sides.

Box side	CTRL	NOCR	NOTER
	Tot flux ($\times 10^{13}$ kg 72 h^{-1}) through A		
A	1.58	1.58	1.37
	% reduced of side A flux		
B	12	7	2.6
C	36	22	2.8
D	41	36	2.9
E	55	55	3.2

occurs from A to B and may be attributable to conversion to precipitation as air is lifted over the warm front (Fig. 15a). The water vapor flux through sides C, D, and E shows passage of the atmospheric river downstream of the Coastal Range and Sierras. The peak values through sides C, D, and E are much less than those upwind of the mountain ranges through side A. Overall, there is a general reduction in water vapor flux values from west to east with the greatest reduction between B and C, which lie on each side of the Coastal Range. The change from C to D across the Sacramento Valley is small, as water vapor is added to the valley from the south. A calculation of fractional reduction from A to E suggests a total decrease of 55% (Table 3). The reduction of water vapor flux from B to E (Table 4), which is analogous to the two-dimensional drying ratio presented earlier, is roughly 49% and consistent with previous studies (Table 1). The Coastal Range and Sierras remove about 28% and 25% of the water vapor flux, respectively (Table 5). The higher magnitude of the water vapor fluxes impinging on the Coastal Range compared to the Sierras contributes to the difference.

The flux through sides H, O, and P represents the along valley flux (Fig. 15b). The flux is down valley (negative values) until ~0900 and 1200 UTC 30 December for P and H, respectively. The flux then becomes up valley (positive) in the Sacramento Valley, while remaining down valley in the San Joaquin through 0200 UTC 31 December, suggesting flow splitting as the flow impinges on the Sierras. A surge of water vapor occurs soon after, indicative of a strong flux of water vapor up the Sacramento Valley. The peak of the water vapor flux through sides H and P occurs around 1200 UTC 31 December, just after the atmospheric river passes by the Petaluma Gap (Fig. 14n), and water vapor is able to flow into the Sacramento Valley unimpeded. The timing of the incursion of the pulse of water vapor from the atmospheric river with the period of the well-developed barrier jet yielded peak up valley fluxes $\sim$370 kg m^{-1} s^{-1} through side H, which is more than half of the cross Sacramento Valley flux through C and D ($\sim$500 kg m^{-1} s^{-1}) for the same time period. The time-integrated flux across H makes up about a quarter of the water vapor lost across the Coastal Range (Fig. 16). The cold-frontal passage can be inferred by a sharp drop in water vapor through side P around 1500 UTC 31 December, as water vapor flux values begin to fall dramatically. As the atmospheric river moves farther south, the up-valley flux through side O increases and peaks around 1800 UTC 31 December. This suggest that water vapor is able to ascend the Santa Lucia range, enter the valley, and is then deflected northward by the higher Sierra Nevada. However, the magnitude of the San Joaquin Valley flux (side O) never reaches the value of the Sacramento Valley fluxes at side H. Finally, all fluxes decrease sharply behind the

TABLE 4. Summary of drying ratios for the CTRL, NOCR, and NOTER runs for box side B and the subsequent downstream sides.

Box side	CTRL	NOCR	NOTER
	Tot flux ($\times 10^{13}$ kg 72 h^{-1}) through B		
B	1.39	1.47	1.33
	% reduced of side B flux		
C	28	16	0.2
D	32	30	0.3
E	49	51	0.7

TABLE 5. Summary of drying ratios for the CTRL, NOCR, and NOTER runs for box side D and the subsequent downstream side.

Box side	CTRL	NOCR	NOTER
	Tot flux ($\times 10^{13}$ kg 72 h^{-1}) through D		
D	0.94	1.02	1.34
	% reduced of side D flux		
E	25	30	1.1

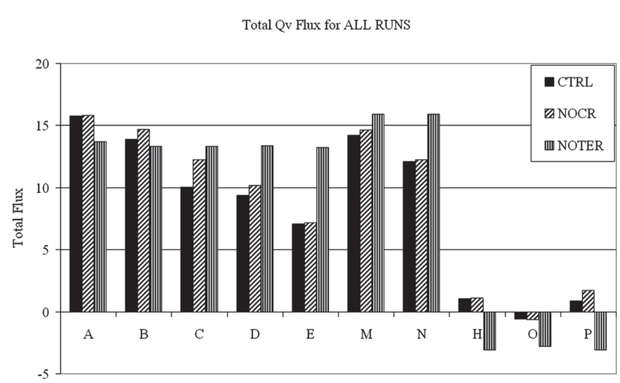

FIG. 16. WRF 72-h total water vapor flux [$\times 10^{12}$ kg (72 h)$^{-1}$] through each box side (A–E, H, M, N, O, and P) for the CTRL, NOCR, and NOTER runs.

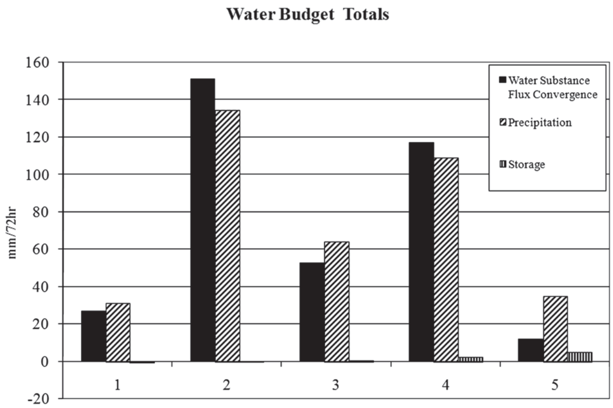

FIG. 17. WRF CTRL run 72-h moisture flux convergence, precipitation, and atmospheric storage for the five boxes labeled in Fig. 3d. Units are mm (72 h)$^{-1}$.

atmospheric river, as the cold front forces the water vapor source southward.

2) Small-scale budget

The small-scale water budget results indicate the relative contributions of water substance convergence, precipitation, and storage (Fig. 17). The budget totals are sensitive to the positioning of the rectangular boxes within the complex terrain. Offshore (box 1) the amount of precipitation is slightly greater than the total convergence. Just downstream, over the Coastal Range (box 2), the precipitation fallout is largest of all the boxes, and as expected, the convergence of water fields is also greatest. Box 4 over the Sierras shows a smaller convergence of water vapor and area-averaged precipitation that is 81% of that over the Coastal Range.

Within the northern portion (box 3) and the southern portion (box 5) of the Sacramento Valley, the water substance flux convergence is less than the amount of precipitation. The northwestern most corner of the box 3 overlaps a portion of an area with heavy precipitation, which may contribute to the imbalance in this box (see Figs. 3c and 11b). Additionally, the eastern sides of boxes 3 and 5 lie along the windward Sierra slopes, where precipitation generation and subsequent flux of hydrometeors downwind yield flux divergence. Storage values, the sum of all of the water substance categories, are greatest over the Sierras, within the southern Sacramento Valley and in the San Joaquin Valley, where residual water vapor from the atmospheric river is largest.

b. No coastal terrain: NOCR

The effects of the Coastal Range are examined in the NOCR run (Figs. 18 and 19). The low-level flow is still southwesterly ahead of the approaching storm, with an anticyclone off the southern California coast (Figs. 18a,b). The atmospheric river approaches as a broad area of water vapor (Fig. 18c), which is lifted along the warm front (Fig. 19a). The atmospheric river is able to penetrate inland to the Sierras, where the flow is deflected to the north toward the Siskiyous. At the base of the Siskiyous the southerly flow converges with water vapor that is transported eastward along the modified base of Siskiyou terrain (Fig. 18d).

The precipitation along the coast is much less with the Coastal Range removed (Fig. 18e). The highest precipitation values are instead located near the concavity formed where the Siskiyous and Sierras meet. Here moist air from directly off the Pacific and air deflected northward by the Sierras persistently converges throughout the run, leading to enhanced precipitation over a small area. Much like the CTRL run, most of the precipitation appears to be driven by orographic effects and locked to the areas of sharp elevation and orographically forced convergence zones.

The water vapor fluxes over the open ocean are nearly identical in the NOCR and CTRL runs (side A in Fig. 20). Closer to the coast, the water vapor flux is higher (side B in Fig. 20) in NOCR than CTRL. More water vapor from the atmospheric river (IWV $>$ 30 mm) is able to reach the coast and penetrate farther inland than in the CTRL run (Fig. 18d). However, the water vapor and low-level flow is still blocked by the Sierras and forced northward. The difference in the CTRL and NOCR water vapor fluxes through side C is the largest of any side. The peak of the flux through side C occurs at the same time in both runs, but the NOCR flux is over 100 kg m^{-1} s^{-1} higher near 0000 UTC 31 December. Inland, there is more flux through side D in the NOCR run, about 50 kg m^{-1} s^{-1} more at the peak. The flux through side E shows almost no difference between the CTRL and NOCR runs, implying nearly equal depletion by the time the air mass reaches the lee of the Sierras in both runs.

The along-valley fluxes are very similar through the southernmost box sides H and O (Fig. 20) in the NOCR run, compared to the respective fluxes in CTRL. The up-valley fluxes are similar in magnitude because the low-level flow is still blocked by the Sierras and forced northward in both CTRL and NOCR runs (Figs. 12d and 18d). There is a substantial increase in water vapor flux through the side P at the base of the Siskiyous in the NOCR run. Water vapor that is able to enter the valley where the Coastal Range used to be is now transported farther north than was the case in the CTRL run (Figs. 19b,d,f).

There is little change in the precipitation total in the over ocean box (box 1) between the NOCR run to the

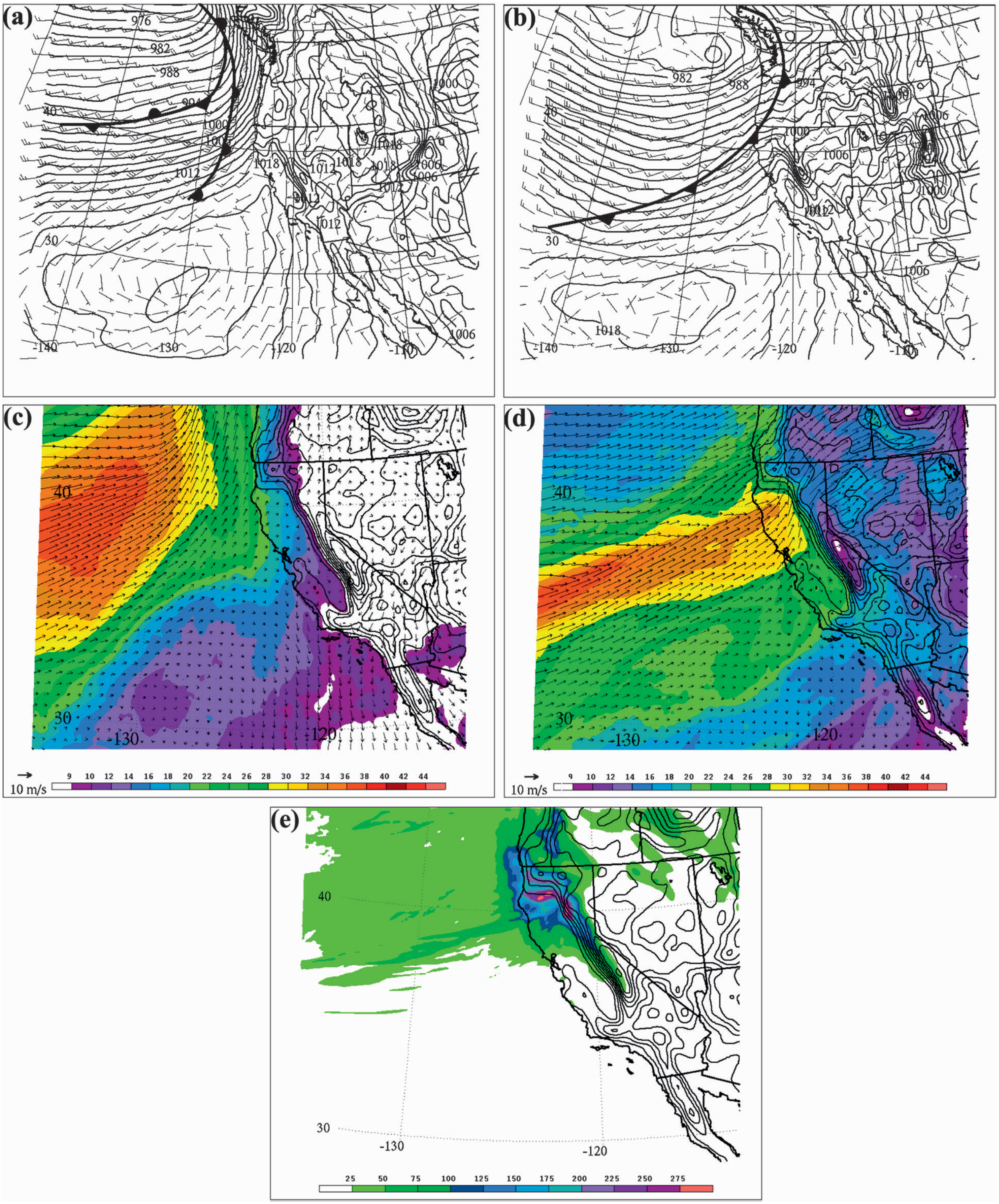

FIG. 18. Plots from the WRF NOCR run: sea level pressure (contours, hPa) and 10-m winds (barbs, m s^{-1}) with surface fronts for (a) 0000 UTC 30 Dec and (b) 0000 UTC 31 Dec 2005. IWV (color shaded, mm) and σ = 0.9205 winds (arrows, m s^{-1}) for (c) 0000 UTC 30 Dec and (d) 0000 UTC 31 Dec 2005. (e) 72-h total precipitation (mm).

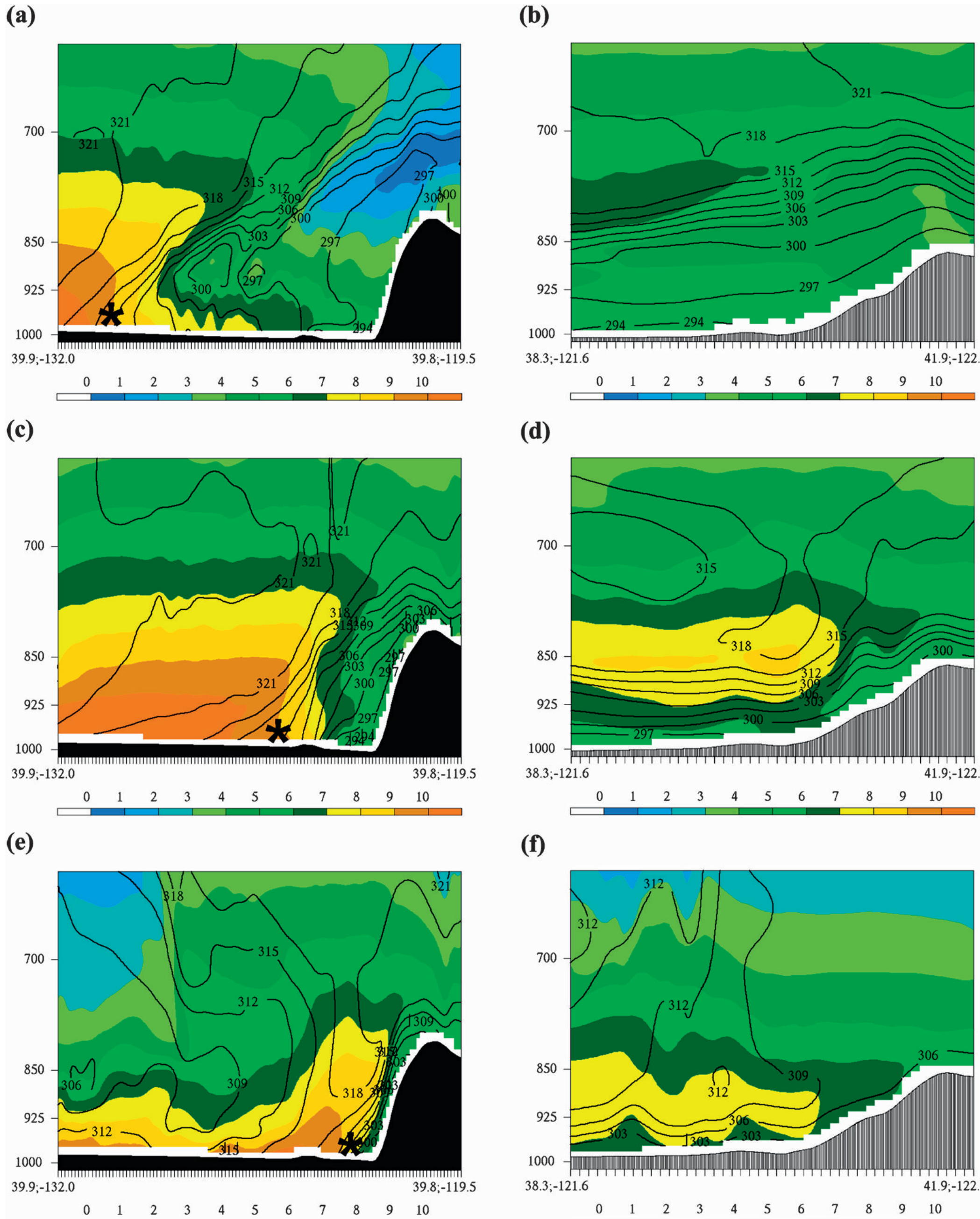

FIG. 19. NOCR WRF cross sections (pressure levels in hPa, labeled on left vertical axis) of equivalent potential temperature (contours, K) and water vapor mixing ratio (color shaded, g kg^{-1}): for cross-section Y (see Fig. 3) at (a) 0000 UTC 30 Dec, (c) 1200 UTC 30 Dec, and (e) 0000 UTC 31 Dec 2005; for cross-section Z at (also see Fig. 3) (b) 1200 UTC 30 Dec, (d) 0000 UTC 31 Dec, and (f) 1800 UTC 31 Dec 2005. Surface warm front denoted by an asterisk in (a),(c), and (e).

CTRL (Fig. 21). In contrast, the precipitation in box 2 is significantly reduced without the Coastal Range. Precipitation totals in boxes 3 and 4 rose in the NOCR run compared to CTRL, with more water vapor reaching the slopes of the Sierras (Figs. 18c,d). Precipitation in the San Joaquin Valley (box 5) increases by 37% between NOCR and CTRL. Most of the increased precipitation occurs at the northern end of the box, adjacent to box 2. More water vapor is available for conversion to precipitation because the northern Coastal Range is gone.

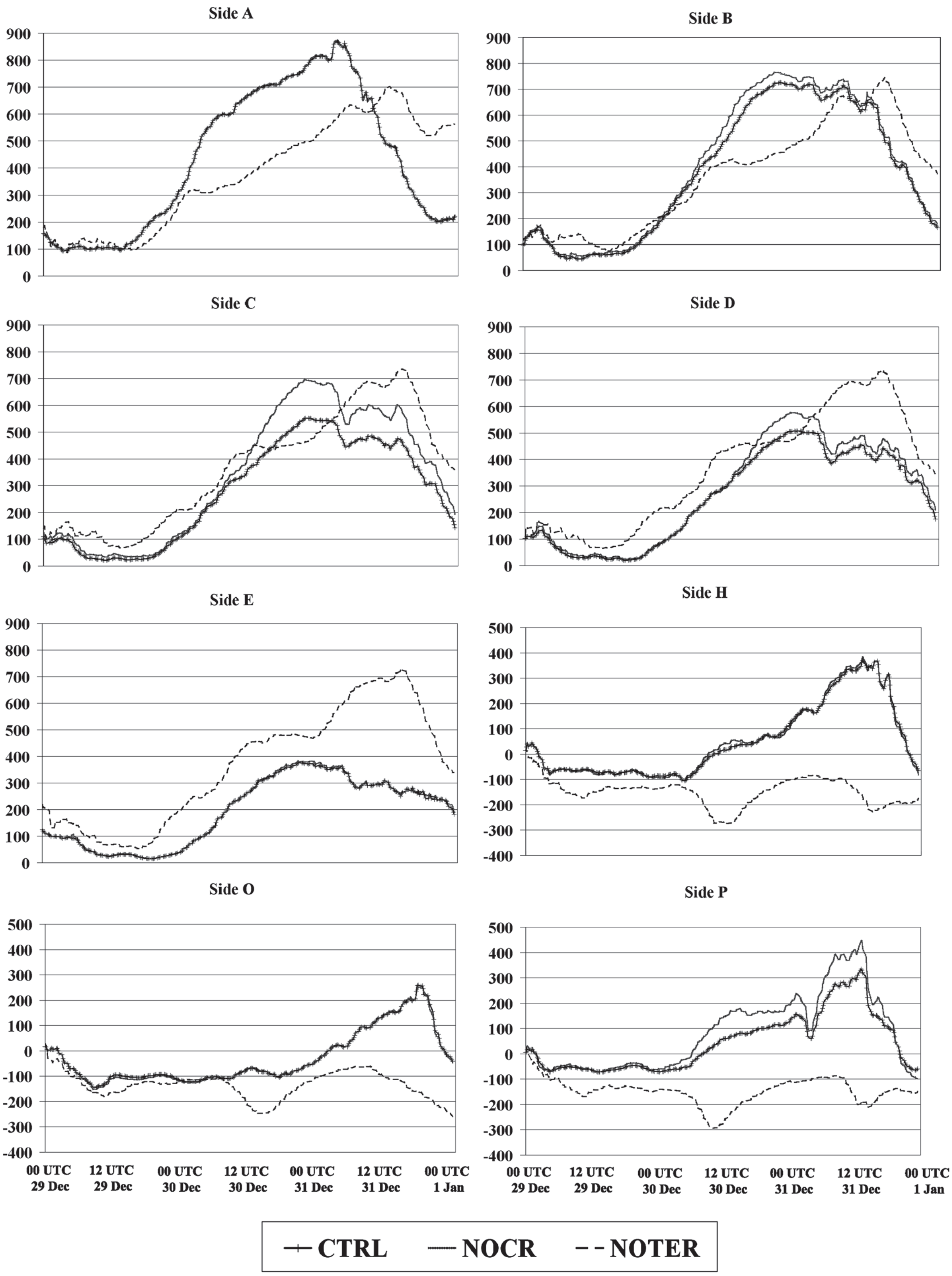

FIG. 20. Comparison of time series of normalized water vapor flux through box sides A, B, C, D, E, H, O, and P for the CTRL, NOCR, and NOTER runs. Flux values (kg m^{-1} s^{-1}) on the vertical axis. Time labels at bottom apply to each panel. [Note: Fluxes for side A, H, and O, are nearly equal for the CTRL and NOCR runs. Fluxes are normalized by the horizontal length (m) of grid boxes.]

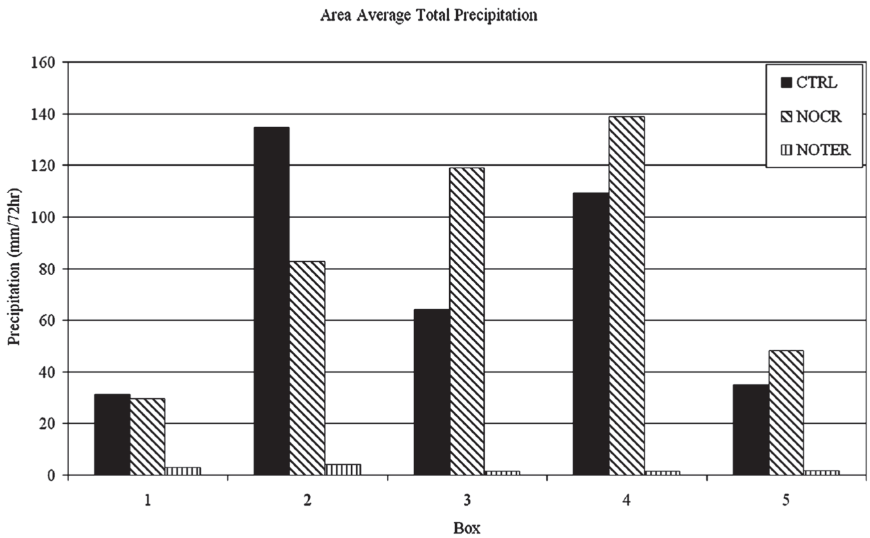

FIG. 21. WRF 72-h area-average total precipitation (mm) in boxes 1–5 for the CTRL, NOTER, and NOCR simulations.

The 72-h total water vapor flux through each box side (Fig. 16) illustrates the relative airmass transformation in the CTRL versus NOCR runs. The additional precipitation at the northern end of the box 3 in NOCR partially compensates for the precipitation in box 2 in CTRL that was not present in NOCR.

c. *No terrain: NOTER*

Removing all the terrain yielded similar total fluxes through box sides A–E (Fig. 16) and a significant reduction of the total precipitation (Fig. 21). The atmospheric river that developed was weaker off shore than in the CTRL run (Fig. 20a), but remained steady, peaking at 700 kg m^{-1} s^{-1} through sides B–E (Fig. 20). The formation of the storm system appears to be different enough from the CTRL run to impact the strength of the LLJ, and therefore, to alter the flux over the ocean. In the CTRL run, there was an anticyclone located off the California coast (Fig. 12b), while in the NOTER run, this anticyclone was shifted east over southern California (Figs. 22a,b). This change in the large-scale flow reduced the water vapor flux offshore by ~200 kg m^{-1} s^{-1}. The bulk of the water vapor, which is similar over the ocean (Fig. 22c), reaches far inland into Nevada (Fig. 22d), unhindered by any terrain, and peaks several hours later than in the CTRL run (side D in Fig. 20), before moving south. As was the case in the NOCR run, there is no Coastal Range to block water vapor (and no Sierras in the NOTER run), allowing the atmospheric river to move inland uniformly. Water vapor flux through sides H, O, and P remain negative through the entire run (Fig. 20). In this case, negative values are not representative of down-valley flux, but instead are a result of the orientation of the box sides and a westerly flow.

The NOTER run produces much less precipitation than the other two runs (Figs. 21 and 22e). With no elevated terrain to force ascent, precipitation is limited mainly to synoptic and frontal forcing. Area-averaged total precipitation shows there is more precipitation over the Coastal Range (box 2) than any other box in the NOTER run (Fig. 21). The 72-h precipitation total from the NOTER run (Fig. 22e) shows an area of increased precipitation along the coast and a generally uniform precipitation distribution inland. Braun et al. (1999b) investigated the role of friction in modifying surface fronts over coastal terrain using idealized simulations. In their simulation with flat terrain, they found that the abrupt increase in surface roughness at the ocean–land boundary led to a narrow zone of upward motion and a weak vertically propagating gravity wave above the coast.

6. Conclusions

Atmospheric rivers accompanying Pacific storm systems play an important role in supplying water vapor to the West Coast. Heavy precipitation associated with these systems falls not only along the west-facing slopes of the Coastal Range, which is subject to the direct landfall of the atmospheric rivers, but also along the windward slopes of the interior mountains. The 29–31 December 2005 storm brought heavy rain and flooding to much of northern California. The atmospheric river strengthened and became more focused as the storm

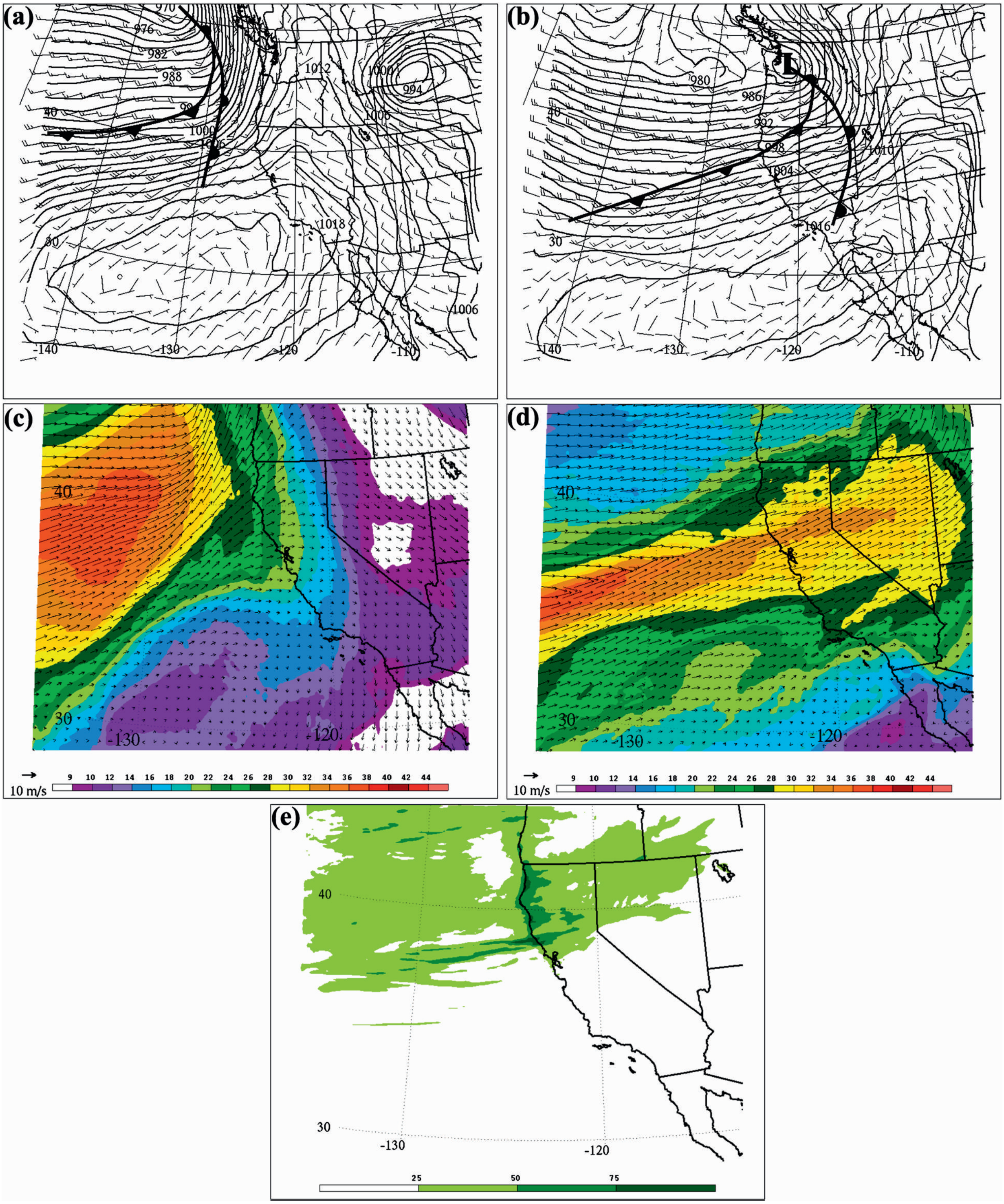

FIG. 22. All plots from the WRF NOTER run: sea level pressure (contours, hPa) and 10-m winds (barbs, m s^{-1}) with surface fronts for (a) 0000 UTC 30 Dec and (b) 0000 UTC 31 Dec 2005. IWV (color shaded, mm) and $\sigma = 0.9205$ winds (arrows, m s^{-1}) for (c) 0000 UTC 30 Dec and (d) 0000 UTC 31 Dec 2005. (e) The 72-h total precipitation (mm).

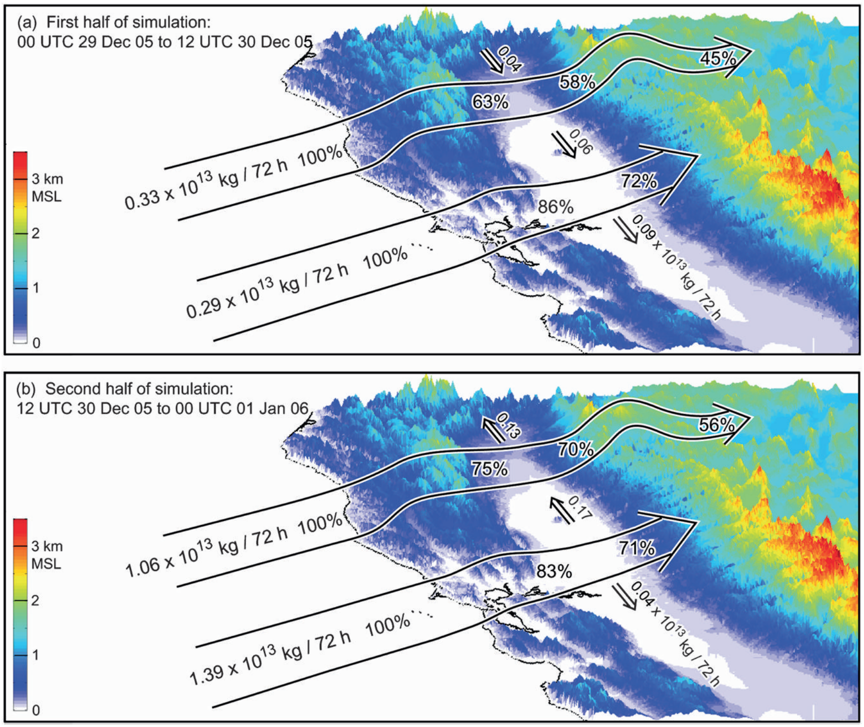

FIG. 23. Conceptual schematic of the predominant airstreams interacting with California's complex terrain (km MSL; see color scale on left) and the associated fractional water vapor fluxes [relative to the fluxes approaching the coast; kg $(72\ \mathrm{h})^{-1}$] for the 29–31 Dec 2005 storm. The flux values were computed similarly to those in Table 2, but that the storm period is split into two parts: (a) 0000 UTC 29 Dec to 1200 UTC 30 Dec 2005 when along barrier flow was northerly and (b) 1200 UTC 30 Dec 2005 to 0000 UTC 1 Jan 2006 when the along barrier flow north of the Petaluma Gap was southerly.

approached the West Coast and made landfall along the northern California coast. Simulations of the storm using the WRF model were able to realistically resolve the structure and strength of the atmospheric river over ocean and land (section 4). The conceptual schematic in Fig. 23 highlights the predominant airstreams interacting with California's complex terrain and their associated fractional water vapor fluxes. While the cross-barrier, southwesterly flow over the Coastal Mountains and Sierras dominates the airmass transformation, the barrier jet at the base of the Sierras yields a small but significant third dimension to the inland movement of water vapor. For this storm, the timing of the peak flow of water vapor through the Petaluma Gap coincides with the period of the strongest barrier jet (Fig. 15). At about 1200 UTC 30 December 2005, the along-barrier flow north of the Petaluma gap switches from northerly to southerly yielding both a source of water vapor at the base of Sisykous at the northern end of the Central Valley and a supplement to the water vapor in the westerly flow over the Sierras. Details of these interactions are summarized below.

In the presence of latent heating (i.e., during saturated conditions), the flow is confined to moist isentropic surfaces, assuming θ_e is conserved to first order. The saturated airstream within the atmospheric river was first slowly lifted along the θ_e surfaces offshore and then rose more steeply over the coastal topography (Fig. 13). The southwesterly water vapor fluxes near the coast peaked near 700 kg $\mathrm{m}^{-1}\ \mathrm{s}^{-1}$. Over land, the Coastal Range caused a significant reduction in the water vapor flux of air entering the Sacramento Valley after crossing the terrain (Figs. 15 and 16). Low-level water vapor flowing inland around the Coastal Range and through the Petaluma Gap into the Sacramento Valley compensates for about a quarter of the water vapor depleted by the westerly flow over the Coastal Range (Table 3–6). Removing the Coastal Range does not appreciably change either the amount of water vapor that enters where the Petaluma Gap would be located or the deflection of low-level water vapor northward by the Sierras.

The barrier jet along the base of the Sierras transported water vapor northward deep into the Sacramento Valley. The timing and magnitude of the up-valley fluxes

TABLE 6. Summary of water substance fluxes for the CTRL, NOCR, and NOTER runs for along-valley fluxes through sides H, O, and P.

Box side	CTRL	NOCR	NOTER
		Tot flux ($\times 10^{13}$ kg 72 h^{-1})	
H	0.16	0.11	−0.00034
O	−0.59	−0.06	−0.00031
P	0.12	0.17	−0.00034

are similar for the CTRL and NOCR runs (Fig. 20). Although the storm-total northward water vapor fluxes are small compared to the southwesterly fluxes, the timing of the incursion of the pulse of water vapor from the atmospheric river with the period when the barrier jet was well developed yielded peak up valley fluxes >300 kg m^{-1} s^{-1} for several hours (Fig. 20). When the Coastal Range is removed, the up-valley flux near the base of the Siskiyous is about 40% larger than in the run with coastal topography (Table 6).

The regional airmass transformation from the coastline to the downwind side of the Sierras near Reno yields a drying ratio of 49% (box sides B–E; Table 4). When examining the impact of the ranges separately, the Coastal Range itself has a drying ratio of 28% (box sides B–C; Table 4), while the Sierras have a drying ratio of 25% (box sides D–E; Table 5). The Sierras remove similar amounts of water vapor in both CRTL and NOCR cases. The regional drying ratio across the entire mountain complex barely changes when the Coastal Range is removed (Table 3).

When all terrain over the West Coast is removed, the synoptic flow develops with a low-level anticyclone located much farther east than observed. The low-level flow between the approaching cyclone and this anticyclone is much weaker, leading to a weaker atmospheric river. Water vapor fluxes in a simulation with no terrain are much weaker over the ocean than in the control simulation (Figs. 16 and 20). The atmospheric river is able to reach far inland into Nevada, and water vapor reduction near the coast is minimal, due mainly to conversion to precipitation by frictional effects along the coast (Fig. 22).

Much of the research on airmass transformation over orography to date has focused on cross-barrier flow often to the exclusion of along-barrier flow. An important question is under what conditions this two-dimensional approximation is more or less valid. For the 29–31 December 2005 Pacific storm, the flow around the coastal terrain and up valley replenished about a quarter of the depleted water vapor lost over the coastal mountains. Further study of the roles of gaps in terrain, the relative timing of pulses of low-level water vapor flux, and the development of the barrier jet is needed to quantify under what sets of synoptic and terrain conditions along-barrier flow is relevant to orographic precipitation processes.

Acknowledgments. Special thanks to Ben Baranowski, Scott Braun, Rob Fovell, Gary Lackmann, Matthew Parker, Heather Reeves, and Dave Spencer for advice and technical help and to two anonymous reviewers for providing insightful comments on the manuscript. This material is based upon work supported by the National Science Foundation under Grant ATM-0544766. Any opinions, findings, and conclusions or recommendations expressed in this material are those of the author(s) and do not necessarily reflect the views of the National Science Foundation.

REFERENCES

Anders, A. M., G. H. Roe, B. Hallet, D. R. Montgomery, N. Finnegan, and J. Putkonen, 2006: Spatial patterns of precipitation and topography in the Himalaya. *Tectonics, Climate and Landscape,* Special Paper 398, S. Willet, N. Brandon, and D. Fiser, Eds., Geological Society of America, 39–53.

——, ——, D. R. Durran, and J. M. Minder, 2007: Scale-scale spatial gradients in climatological precipitation on the Olympic peninsula. *J. Hydrometeor.,* **8,** 1068–1081.

Bao, J.-W., S. A. Michelson, P. J. Neiman, F. M. Ralph, and J. M. Wilczak, 2006: Interpretation of enhanced integrated water-vapor bands associated with extratropical cyclones: Their formation and connection to tropical moisture. *Mon. Wea. Rev.,* **134,** 1063–1080.

Bevis, B. G., S. Bussinger, T. A. Herring, C. Rocken, R. A. Anthes, and R. H. Ware, 1992: GPS meteorology: Remote sensing of atmospheric water vapor using the Global Positioning System. *J. Geophys. Res.,* **97,** 15 787–15 801.

Bond, N. A., and Coauthors, 1997: The Coastal Observation and Simulation with Topography (COAST) experiment. *Bull. Amer. Meteor. Soc.,* **78,** 1941–1955.

Braun, S. A., 2006: High-Resolution simulation of Hurricane Bonnie (1998). Part II: Water budget. *J. Atmos. Sci.,* **63,** 43–64.

——, R. Rotunno, and J. B. Klemp, 1999a: Effects of coastal orography on landfalling cold fronts. Part I: Dry, inviscid dynamics. *J. Atmos. Sci.,* **56,** 517–533.

——, ——, and ——, 1999b: Effects of coastal orography on landfalling cold fronts. Part II: Effects of surface friction. *J. Atmos. Sci.,* **56,** 3366–3384.

Browning, K. A., 1990: Organization of clouds and precipitation in extratropical cyclones. *Extratropical Cyclones: The Erik Palman Memorial Volume,* C. W. Newton and E. Holopainen, Eds., Amer. Meteor. Soc., 129–153.

Buzzi, A., N. Tartaglione, and P. Malguzzi, 1998: Numerical simulations of the 1994 Piedmont flood: Role of orography and moist processes. *Mon. Wea. Rev.,* **126,** 2369–2383.

Carlson, T. N., 1980: Airflow through midlatitude cyclones and the comma cloud pattern. *Mon. Wea. Rev.,* **108,** 1498–1509.

Didlake, A. C., Jr., 2007: An analysis of water vapor flux and orographic precipitation in Northern California. B.S. thesis, Dept. of Geology and Geophysics, Yale University, 47 pp.

Doswell, C. A., C. Ramis, R. Romero, and S. Alonso, 1998: A diagnostic study of three heavy precipitation episodes in the western Mediterranean region. *Wea. Forecasting,* **13,** 102–124.

Ecklund, W. L., D. A. Carter, and B. B. Balsley, 1988: A UHF wind profiler for the boundary layer: Brief description and initial results. *J. Atmos. Oceanic Technol.,* **5,** 432–441.

Galewsky, J., and A. Sobel, 2005: Moist dynamics and orographic precipitation in northern and central California during the New Year's Flood of 1997. *Mon. Wea. Rev.,* **133,** 1594–1612.

Grubišić, V., R. K. Vellore, and A. W. Huggins, 2005: Quantitative precipitation forecasting of wintertime storms in the Sierra Nevada: Sensitivity to microphysical parameterization and horizontal resolution. *Mon. Wea. Rev.,* **133,** 2834–2859.

Hahn, R. S., and C. F. Mass, 2009: The impact of positive-definite moisture advection and low-level moisture flux bias over orography. *Mon. Wea. Rev.,* **137,** 3055–3071.

Heggli, M. F., and R. M. Rauber, 1988: The characteristics and evolution of super-cooled water in winter time storms over the Sierra Nevada: A summary of microwave radiometric measurements taken during the Sierra Cooperative Pilot Project. *J. Appl. Meteor.,* **27,** 989–1015.

Lackmann, G., and J. Gyakum, 1999: Heavy cold-season precipitation in the northwestern United States: Synoptic climatology and an analysis of the flood of 17–18 January 1986. *Wea. Forecasting,* **14,** 687–700.

Lin, Y.-L., S. Chiao, T.-A. Wang, M. L. Kaplan, and R. Weglarz, 2001: Some common ingredients for heavy orographic precipitation. *Wea. Forecasting,* **16,** 633–660.

Marwitz, J. D., 1983: The kinematics of orographic airflow during Sierra storms. *J. Atmos. Sci.,* **40,** 1218–1227.

——, 1986: A comparison of winter orographic storms over the San Juan Mountains and the Sierra Nevada. *Precipitation Enhancement—A Scientific Challenge, Meteor. Monogr.,* No. 43, Amer. Meteor. Soc., 109–113.

——, 1987: Deep orographic storms over the Sierra Nevada. Part I: Thermodynamic and kinematic structure. *J. Atmos. Sci.,* **44,** 159–185.

Minder, J. R., D. R. Durran, G. H. Roe, and A. M. Anders, 2008: The climatology of small-scale orographic precipitation over the Olympic Mountains: Patterns and processes. *Quart. J. Roy. Meteor. Soc.,* **134,** 817–839.

Mesinger, F., and Coauthors, 2006: North American Regional Reanalysis. *Bull. Amer. Meteor. Soc.,* **87,** 343–360.

Neiman, P. J., F. M. Ralph, A. B. White, D. E. Kingsmill, and P. O. G. Persson, 2002: The statistical relationship between upslope flow and rainfall in California's coastal mountains: Observations during CALJET. *Mon. Wea. Rev.,* **130,** 1468–1492.

——, B. E. Martner, A. B. White, G. A. Wick, F. M. Ralph, and D. E. Kingsmill, 2005: Wintertime nonbrightband rain in California and Oregon during CALJET and PACJET: Geographic, interannual, and synoptic variability. *Mon. Wea. Rev.,* **133,** 1199–1223.

——, F. M. Ralph, A. B. White, J. D. Lundquist, and M. D. Dettinger, 2008: Meteorological characteristics and overland precipitation impacts of atmospheric rivers affecting the west coast of North America based on eight years of SSM/I satellite observations. *J. Hydrometeor.,* **9,** 22–47.

Parish, T. R., 1982: Barrier winds along the Sierra Nevada Mountains. *J. Appl. Meteor.,* **21,** 925–930.

Pierrehumbert, R. T., and B. Wyman, 1985: Upstream effects of mesoscale mountains. *J. Atmos. Sci.,* **42,** 977–1003.

Ralph, F. M., P. J. Neiman, and T. L. Keller, 1999: Deep-tropospheric gravity waves created by leeside cold fronts. *J. Atmos. Sci.,* **56,** 2986–3009.

——, ——, and G. A. Wick, 2004: Satellite and CALJET aircraft observations of atmospheric rivers over the eastern North Pacific Ocean during the winter of 1997/98. *Mon. Wea. Rev.,* **132,** 1721–1745.

——, ——, and R. Rotunno, 2005: Dropsonde observations in low-level jets over the northeastern Pacific Ocean from CALJET-1998 and PACJET-2001: Mean vertical profile and atmospheric river characteristics. *Mon. Wea. Rev.,* **133,** 889–910.

Rauber, R. M., 1992: Microphysical structure and evolution of a Sierra Nevada shallow orographic cloud system. *J. Appl. Meteor.,* **31,** 3–24.

Reeves, H. D., and Y. L. Lin, 2008: Dynamic forcing and mesoscale variability of heavy precipitation events over the Sierra Nevada Mountains. *Mon. Wea. Rev.,* **136,** 62–77.

Reynolds, D. W., and A. S. Dennis, 1986: A review of the Sierra Cooperative Pilot Project. *Bull. Amer. Meteor. Soc.,* **67,** 513–523.

Rotunno, R., and R. Ferretti, 2001: Mechanisms of intense Alpine rainfall. *J. Atmos. Sci.,* **58,** 1732–1749.

Skamarock, W. C., 2006: Positive-definite and montonic limiters for unrestricted-time step transport schemes. *Mon. Wea. Rev.,* **134,** 2241–2250.

——, and J. B. Klemp, 2008: A time-split nonhydrostatic atmospheric model for research and NWP applications. *J. Comput. Phys.,* **227,** 3465–3485.

——, and M. L. Weisman, 2009: The impact of positive-definite moisture transport on NWP precipitation forecasts. *Mon. Wea. Rev.,* **137,** 488–494.

——, J. B. Klemp, J. Dudhia, D. O. Gill, D. M. Barker, W. Wang, and J. G. Powers, 2005: A description of the Advanced Research WRF version 2. NCAR Tech. Note, NCAR/TN-468+STR, 88 pp. [Available from UCAR Communications, P.O. Box 3000, Boulder, CO 80307.]

Smith, R. B., and J. P. Evans, 2007: Orographic precipitation and water vapor fractionation over the southern Andes. *J. Hydrometeor.,* **8,** 3–19.

——, Q. Jiang, M. G. Fearon, P. Tabary, M. Dorninger, J. D. Doyle, and R. Beniot, 2003: Orographic precipitation and air mass transformation: An Alpine example. *Quart. J. Roy. Meteor. Soc.,* **129,** 433–454.

——, I. Barstard, and L. Bonneau, 2005: Orographic precipitation and Oregon's climate transition. *J. Atmos. Sci.,* **62,** 177–191.

Smolarkiewicz, P. K., and R. Rotunno, 1990: Low Froude number flow past three-dimensional obstacles. Part II: Upwind flow reversal zone. *J. Atmos. Sci.,* **47,** 1498–1511.

Strangeways, I. C., 1996: Back to basics: the 'met. enclosure': Part 2(b)—Raingauges, their errors. *Weather,* **51,** 298–303.

Weber, B. L., D. B. Wuertz, D. C. Welsh, and R. McPeek, 1993: Quality controls for profiler measurements of winds and RASS temperatures. *J. Atmos. Oceanic Technol.,* **10,** 452–464.

Wentz, F. J., 1997: A well-calibrated ocean algorithm for SSM/I. *J. Geophys. Res.,* **102,** 8703–8718.

White, A. B., P. J. Neiman, R. M. Ralph, D. E. Kingsmill, and P. O. G. Persson, 2003: Coastal orographic rainfall processes observed by radar during the California LandFalling Jets Experiment. *J. Hydrometeor.,* **4,** 264–282.

Zhu, Y., and R. E. Newell, 1998: A proposed algorithm for moisture fluxes from atmospheric rivers. *Mon. Wea. Rev.,* **126,** 725–735.